The magmatic conditions and hypersolidus deformation of lower crustal magma chamber below a fast-spreading ridge — Insight from the core analyses of the Oman ICDP drill holes GT1A & GT2A

Trinh NGUYEN[1], Susumu UMINO[1,*], Osamu ISHIZUKA[2], Yuki KUSANO[2], Takahiro FUDAI[1], Akihiro TAMURA[1] and Norikatsu AKIZAWA[3]

[1]Division of Natural System, Graduate School of Natural Science and Technology, Kanazawa University
Kanazawa, 920-1192, Japan
[2]National Institute of Advanced Industrial and Science Technology
Tokyo 100-8921 Japan
[3]Atmosphere and Ocean Research Institute, The University of Tokyo
Chiba 277-8563, Japan

Abstract   The ICDP Oman Drilling Project drilled the lower crustal section of the Oman ophiolite in Wadi Gideah, north of Ibra and recovered 400 m long cores each from Hole GT1A and GT2A. The microstructures of cumulus crystals were described, the chemical compositions of whole-rock and minerals were analyzed, and the amounts of trapped melt between cumulates were estimated that help to reveal the magmatic conditions and hypersolidus deformation operated in the lower crustal magma chamber beneath the Oman paleoridge axis. Progressive downhole variations in cumulate gabbro microstructures are observed throughout the hole GT2A to GT1A. Plagioclase changes from flat, platy crystals with high aspect ratios to short, stubby crystals with wavy outlines. Clinopyroxene is deformed to distorted rectangular shapes with a quarter structure, and then changes into crystals with sub-grains, which eventually forms neoblasts. These textural changes indicate the progressive downhole deformation under submagmatic conditions, followed by subsolidus crystal lattice deformation, most likely caused by the compaction of crystal mush. The consistently low trapped melt fractions (TMFs) (< 5 mass%) throughout the two drill holes indicate that the crystal mush reached its maximum compaction.

The whole-rock compositions plot within a quadrilateral connecting cumulus olivine, plagioclase, clinopyroxene and a small amount of melt of primitive V1 sheeted dikes indicated by TMFs. Rare earth element compositions of melts in equilibrium with clinopyroxene cores are generally identical to those of the V1 sheeted dikes, but some equilibrium melts with GT1A clinopyroxene are more primitive than the sheeted dikes. The whole-rock and mineral compositions show no differentiation trend with stratigraphy, but are variable within a range in Hole GT2A and GT1A except in the upper 200 m of Hole GT2A. Ophitic clinopyroxenes common in both holes irrespective to the stratigraphic levels require a large degree of supercooling for their formation. This indicates that ophitic clinopyroxenes crystallized in the uppermost axial melt lens, and were transported downward with the subsiding crystal mush in the lower crust.

_____

  * *Corresponding author*   E-mail: sesumin@staff.kanazawa-u.ac.jp

2   The magmatic conditions and hypersolidus deformation of lower crustal magma chamber
below a fast-spreading ridge — Insight from the core analyses of the Oman ICDP drill holes GT1A
& GT2A

1   Introduction

The architecture of the upper oceanic crust spread at intermediate and fast rates has been observed in some tectonic windows by submersible dives and directly sampled by ocean floor drilling, which confirmed the stratigraphy of basalt lavas and volcaniclastic rocks underlain by the sheeted dike complex (Alt et al., 1993; Karson, 2002; Teagle et al., 2012). However, the lower oceanic crust is much less accessible and only partially exposed and sampled. Well known examples are some oceanic core complexes formed along slow-spreading ridges such as the Atlantis Bank on the Southwest Indian Ridge (Dick et al., 2000), and the Atlantis Massif on the Mid-Atlantic Ridge (Blackman et al., 2011), where the lower crustal gabbros are largely exposed and were sampled by lengthy drill cores more than 1400 m. Compared with the slow-spread crust, exposures of the lower crust formed at fast-spreading ridges are fewer in number and limited in some tectonic windows such as the Hess Deep and the Pito Deep (Karson, 2002), where only 100–900 m of the uppermost lower crust were sampled (Gillis et al., 1993; Perk et al., 2007).   Only one drill hole 1256D reached the intact uppermost gabbro-sheeted dikes transition, where two vari-textured gabbro bodies, 52 m thick and 24 m thick each, intruded and thermally metamorphosed the screen rocks of granoblastic dikes (Teagle et al., 2012). However, the lower crustal cumulates are yet to be reached. Modally layered gabbros resembling those comprising the lower crustal sections of some ophiolites were first drilled at Site 1415 in the Hess Deep rift (Gillis et al., 2014). Although the presence of non-dynamic layering and irregular banding in those layered gabbros are much less common in layered gabbros from the Oman Ophiolite, a centimeter-scale, modal layering subparallel to a strong foliation of the Hess Deep gabbro confirm a long-held belief that such rocks exist in the lower crust.

The lower crustal gabbros of the Oman Ophiolite show lithological variations in descending order from vari-textured gabbros with heterogeneous grain size and hydrous minerals through foliated gabbros with steep planer foliation that are occasionally truncated and tightly folded to layered gabbros with subhorizontal modal layering parallel to the Moho (Nicolas and Boudier, 2015). The vari-textured upper gabbros are isotropic and lack a preferred mineral orientation, which are interpreted to be a frozen melt lens beneath the sheeted dike complex (MacLeod and Yaouancq, 2000). Foliated gabbros develop a moderate foliation and lineation with a shape-preferred orientation of crystals but with a limited intracrystalline strain (Nicolas and Boudier, 2015; Cheadle and Gee, 2017). Steeply dipping foliation is ascribed to hypersolidus deformation during subsidence and subsequent lateral transportation of crystal mush layers, which initially accumulated on the floor of melt lens below the sheeted dike complex (Nicolas and Boudier, 2015). Such a magma chamber composed largely of crystal mush is called a gabbro glacier (Quick and Denlinger, 1993). In contrast, layering of the layered gabbros are characterized by modal grading with stretched olivine aggregates subparallel to the high-temperature plastic flow in the underlying mantle. Kelemen and Aharonov (1998) stressed the role of permeability barriers that block porous melt ascent from the uppermost mantle through the lower crust, resulting in the formation of gabbroic sills and impregnated peridotites within the Moho transition zone (MTZ) and the lower crustal layered gabbros. Modal layering is caused by periodic changes in magma pressure due to the accumulation and discharge of melt in the sill. This is called the sheeted sill model (Kelemen and Aharonov, 1998).

Perk et al. (2007) proposed that a robust magma supply and/or a weak hydrothermal circulation would less efficiently cool the axial magma chamber to develop thick crystal mush in the lower crust. These conditions favor the formation of gabbro glaciers. In contrast, when the magma supply is low and/or hydrothermal circulation is intense, the magma chamber cools efficiently to form thin mushy portion underlain by ridged lower crust with some melt lenses. This tends to produce magma sills, resulting in the development of layered gabbros. Slow cooling will promote compaction and squeezing of interstitial melt out of the subsiding mush, whereas the rapidly cooled mush will freeze more interstitial melt trapped between cumulus minerals (Perk et al., 2007). Therefore, trapped melt fractions (TMFs) would be key to identify the thermal state of the lower crustal magma chambers.

The International Continental Scientific Drilling Program (ICDP) Oman Drilling Project drilled two holes GT1A and GT2A into the lower crustal section of the Oman Ophiolite in Wadi Gideah, north of Ibra (Kelemen et al, 2020b, c; Figure 1). Hole GT1A and GT2A targeted layered gabbros and the transition from foliated to layered gabbros, respectively, and each recovered 400-m long cores of gabbros. These holes are ideal for testing whether there are any systematic differences in TMF between the gabbroic cores from the two drill holes. This study focuses on estimating TMFs between cumulus minerals in the GT1A and GT2A cores and how they vary with the textural variations associated with deformation and subsequent recrystallization of cumulus minerals.

2 Geology and the ICDP drilling of the lower crustal section in Wadi Gideah

The Oman-United Arab Emirates (Oman-UAE) ophiolite is a member of the long chain of the Tethyan ophiolites that extends from the western Mediterranean to the Far East. The diachroneity and periodicity in the ophiolite formation along the Tethyan ophiolites suggest the opening and closing of ocean basins in the Mesozoic (Smith, 1971). The Oman-UAE ophiolite is a paleoridge system that extends 500 km in length and 50-100 km in width. This is the largest and best-preserved ophiolite in the world that detached from the ocean floor and obducted onto the Arabian margin by 70±5 Ma during late Cretaceous. The ophiolite structure is proposed to be of a fast-spread ridge system based on the ca. 50-km spacing of mantle diapirs and paleoridge segment boundaries. This is inferred from the microstructures of the mantle peridotites, thickness of the Moho transition zone, duplicated upper crust stratigraphy, mutually intrusive sheeted dikes and the intrusive relationships of lower crustal gabbros of MORB affinity (MacLeod and Rothery, 1992; Nicolas et al., 2000; Adachi and Miyashita, 2003; Miyashita et al., 2003; Umino et al., 2003). This is in agreement with the estimated half-spreading rate of 50–100 mm/a by using zircon U-Pb dating (Rioux et al., 2012, 2013; Nicolas and Boudier, 2015). The southeastern and central part of the ophiolite, from Wadi Tayin to Haylayn and Sarami massifs, comprises ridge segments about 40-50 km wide and over 200 km long NW-SE, which opened up in the NE-SW direction 1–2 Myr older lithosphere formed at a NE–SW-striking ridge axis.

Wadi Gideah in the southern Wadi Tayin massif about 10 km north of the town of Ibra preserves an almost complete oceanic crustal section of the ophiolite (Figure 1) (Pallister and Hopson, 1981; Nicolas et al., 2000; 2015; Koepke et al., 2022). The southerly inclined crustal sequence exposes the gabbros and mantle peridotites to the north, while upper crustal sequence exposes sheeted dikes as small hills and sporadic remnants of pillow basalts in the south. The paleoridge axis runs subparallel to the wadi 2 km to the east and extends to the diapiric structure of the mantle peridotite, indicating that the Wadi Gideah section represents the lower crustal section in the paleoridge segment center (Nicolas et al., 2000; Nicolas and Boudier, 2015). The Oman Drilling

4   The magmatic conditions and hypersolidus deformation of lower crustal magma chamber
below a fast-spreading ridge ─ Insight from the core analyses of the Oman ICDP drill holes GT1A
& GT2A

Project drilled into the lower and middle plutonic sections at GT1A and GT2A in Wadi Gideah, respectively. Petrographic descriptions and the whole-rock geochemistry are reported in the Proceedings of the Oman Drilling Project (Kelemen et al., 2020a, b, c) and are briefly summarized below;
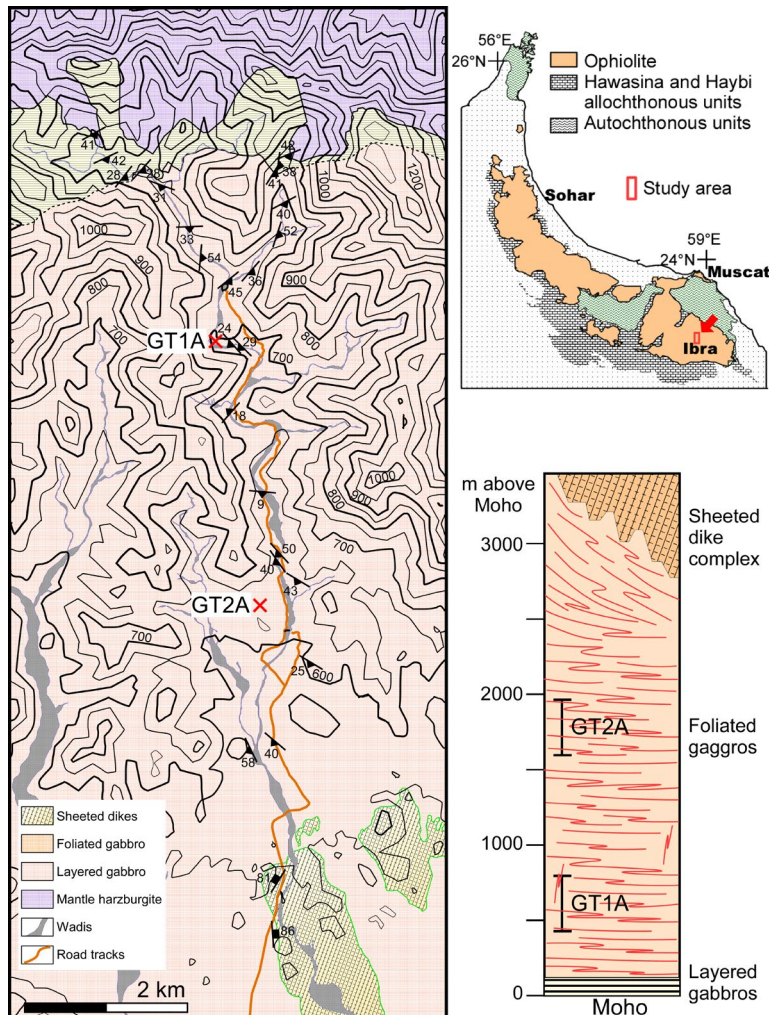
Figure 1. Lithological map and columner section along Wadi Gideah showing planer structures (foliation, layering, intrusive contact) of gabbros and sheeted dikes (this study). Localities and stratigraphic levels of Hole GT1A and GT2A are shown.

Site GT1A (22.890°N, 58.520°E) was intended to drill into the lower layered gabbros. Almost all gabbros in the outcrops around this site are desert-varnished by weathering. Layering with very limited crystal-plastic deformation, and fault zones with both normal and reverse shears were observed in Hole GT1A. The main lithology in Hole GT1A is olivine gabbro and olivine-bearing gabbro, followed by minor rock types including olivine melagabbro, orthopyroxene-bearing olivine gabbro, oxide-bearing olivine gabbro, gabbro, anorthositic gabbro, troctolitic gabbro, orthopyroxene-bearing gabbro, gabbronorite and dunite. The most common rock type, olivine gabbro, displays a wide range of the bulk Mg# (74.8–83.7), Ca# (95.2–98.3) (Mg# = molar ratios of Mg/(Mg + Fe$_{Total}$) × 100, and Ca# = molar ratio Ca/(Ca + Na) × 100) and Cr and Y concentrations (116–1974 and 1.3–6.8 μg/g, respectively). GT1A gabbros range 10.2–18.6 mass% CaO and 7.6–28.3 mass% Al$_2$O$_3$. Positive Eu anomalies in primitive-mantle normalized

rare earth elements indicate the accumulation of plagioclase. Depleted light REEs indicate that these rocks are cumulates derived from magmas formed by partial melting of the mantle.

Site GT2A (22.863°N, 58.520°E) is located about 4 km to the south of Hole GT1A. This site aimed to drill from the upper foliated gabbros to the lower layered gabbros. Various structures observed in this hole are almost similar to Hole GT1A, including layering, faults and limited crystal-plastic deformation. The lithology is also similar to Hole GT1A, including olivine gabbro, olivine-bearing gabbro, and olivine melagabbro, followed by other minor rock types such as gabbro, gabbronorite, vari-textured gabbro. troctolite, anorthositic gabbro, and troctolitic gabbro. Comparing olivine gabbro and olivine-bearing gabbro between 2 holes, GT2A rocks are more evolved with lower Mg#, Ca#, Cr, Ni, V, and Y contents. The most common rock type of olivine gabbro displays a wide range of differentiation in Mg# (54.8–81.2), Ca# (90.9–98.3) and Cr and Y concentrations (Cr = 19–1576 μg/g; Y = 3.6–8.6 μg/g). All rock types in GT2A have CaO and Al_2O_3 in the range of 8–19.5 mass% and 11.0–31.0 mass%, respectively. There is less evidence for accumulation of plagioclase and olivine in Hole GT2A than in Hole GT1A. Positive Eu and Sr anomalies in primitive-mantle normalized plots indicate plagioclase accumulation, although it is less than in Hole GT1A as shown by the lower Eu anomalies for Hole GT2A. The more differentiated nature of the Hole GT2A rocks is indicated by the higher concentrations of REEs in Hole GT2A than Hole GT1A like major elements (Kelemen et al., 2020a, b, c).

3   Methods

Textural observations

Core samples were made into sets of two thin sections; one was cut parallel to the foliation of constituent minerals, and the other was normal to the foliation and parallel to the lineation. Plagioclase and clinopyroxene crystals were divided into several types based on their crystal morphology and the mutual relationships as defined in Chapter 4.1. The number of each crystal type was counted along lines set normal to the foliation on the thin sections. A total of 1 to 188 crystals were counted per thin section (Table 1). Primary plagioclase grains cut normal to twinning planes were selected and the aspect ratios were determined by measuring long and short axes. About 10 plagioclase grains were measured from each thin section to calculate the average aspect ratio.

Table 1. Frequency of shape types of cumulus plagioclase and clinopyroxene from Hole GT1A and GT2A. mbs: meters below surface.

Hole_Core_Section_Interval	mbs Top	mbs Bottom	Plag Primary no	Plag Primary %	Plag Broken no	Plag Broken %	Plag Equilibrated no	Plag Equilibrated %	Plag Total no	Plag Total %	Cpx Primary no	Cpx Primary %	Cpx Subgrain no	Cpx Subgrain %	Cpx Neoblast no	Cpx Neoblast %	Cpx Equilibrated no	Cpx Equilibrated %	Cpx Total no	Cpx Total %
Hole GT1A																				
GT1A_30_4_59-63	72.75	72.79	8	7.0	100	87.0	7	6.1	115	100.0	58	90.6	6	9.4	0	0.0	0	0.0	64	100.0
GT1A_33_3_20-24	80.60	80.64	9	6.7	117	86.7	9	6.7	135	100.0	67	87.0	10	13.0	0	0.0	0	0.0	77	100.0
GT1A_38_1_52-56	91.67	91.71	7	6.4	94	86.2	8	7.3	109	100.0	103	87.3	15	12.7	0	0.0	0	0.0	118	100.0
GT1A_41_3_33-37	99.34	99.38	6	6.3	82	86.3	7	7.4	95	100.0	129	86.6	20	13.4	0	0.0	0	0.0	149	100.0
GT1A_45_2_43-47	104.72	104.76	7	6.3	96	85.7	9	8.0	112	100.0	84	86.6	9	9.3	4	4.1	0	0.0	97	100.0
GT1A_83_4_20-24	208.46	208.50	3	2.3	116	87.9	13	9.8	132	100.0	97	78.9	14	11.4	9	7.3	3	2.4	123	100.0
GT1A_88_3_21-25	220.15	220.19	2	2.1	84	88.4	9	9.5	95	100.0	70	76.9	11	12.1	8	8.8	2	2.2	91	100.0
GT1A_95_2_38-42	237.17	237.21	2	1.2	148	89.2	16	9.6	166	100.0	130	75.1	22	12.7	15	8.7	6	3.5	173	100.0
GT1A_122_3_11-15	309.14	309.18	1	0.8	115	92.0	9	7.2	125	100.0	96	69.1	17	12.2	19	13.7	7	5.0	139	100.0
GT1A_147_1_3-7	374.83	374.87	1	0.8	108	90.8	10	8.4	119	100.0	78	61.9	15	11.9	19	15.1	14	11.1	126	100.0
GT1A_152_4_13-17	392.47	392.51	1	0.6	141	91.0	13	8.4	155	100.0	63	60.0	14	13.3	25	23.8	3	2.9	105	100.0
GT1A_154_4_61-65	399.14	399.18	1	0.6	155	90.6	15	8.8	171	100.0	61	59.8	22	21.6	17	16.7	2	2.0	102	100.0
GT1A_156_1_53-57	402.78	402.82	1	0.6	153	90.5	15	8.9	169	100.0	68	59.6	25	21.9	20	17.5	1	0.9	114	100.0
Hole GT2A																				
GT2A_20_3_55-59	44.47	44.51	56	73.7	20	26.3	0	0.0	76	100.0	50	98.0	1	2.0	0	0.0	0	0.0	51	100.0
GT2A_35_3_71-75	90.08	90.12	21	16.5	103	81.1	3	2.4	127	100.0	95	94.1	6	5.9	0	0.0	0	0.0	101	100.0
GT2A_46_3_56-60	120.30	120.34	11	12.0	78	84.8	3	3.3	92	100.0	159	91.9	14	8.1	0	0.0	0	0.0	173	100.0
GT2A_46_4_47-51	121.17	121.21	9	11.4	66	83.5	4	5.1	79	100.0	97	91.5	9	8.5	0	0.0	0	0.0	106	100.0
GT2A_50_1_47-51	130.75	130.79	7	12.3	47	82.4	3	5.3	57	100.0	117	91.4	11	8.6	0	0.0	0	0.0	128	100.0
GT2A_52_3_25-29	138.31	138.35	17	12.2	119	85.6	3	2.2	139	100.0	102	91.9	9	8.1	0	0.0	0	0.0	111	100.0
GT2A_75_3_8-12	196.52	196.56	18	10.1	158	88.3	3	1.7	179	100.0	152	91.6	14	8.4	0	0.0	0	0.0	166	100.0
GT2A_86_2_33-37	229.03	229.07	14	9.1	137	89.0	3	1.9	154	100.0	52	91.2	2	3.5	3	5.3	0	0.0	57	100.0
GT2A_102_1_3-7	273.88	273.92	5	3.6	127	92.7	5	3.6	137	100.0	137	87.3	16	10.2	4	2.5	0	0.0	157	100.0
GT2A_104_1_5-9	280.00	280.04	6	3.2	175	93.1	7	3.7	188	100.0	118	85.5	13	9.4	7	5.1	0	0.0	138	100.0
GT2A_104_4_53-57	282.73	282.77	9	5.9	141	92.8	2	1.3	152	100.0	72	84.7	7	8.2	6	7.1	0	0.0	85	100.0
GT2A_105_2_39-43	284.25	284.29	5	2.9	161	93.6	6	3.5	172	100.0	86	82.7	4	3.8	12	11.5	2	1.9	104	100.0
GT2A_117_2_6-10	314.34	314.38	3	2.7	105	93.8	4	3.6	112	100.0	105	78.9	10	7.5	12	9.0	6	4.5	133	100.0
GT2A_151_3_18-22	406.24	406.28	1	0.8	120	96.8	3	2.4	124	100.0	73	75.3	13	13.4	11	11.3	0	0.0	97	100.0

Whole-rock major and trace element analyses by XRF and ICP-MS

Eighteen of GT1A and thirteen of GT2A core samples were chosen for whole-rock analyses. Whole-rock major elements were analyzed by X-ray fluorescence method using a ZSX primus II at the College of Science and Engineering, Kanazawa University, Japan (Table 2). Whole-rock trace elements were determined at the Geological Survey of Japan by an inductively coupled plasma mass spectrometry (ICP-MS) on a VG Platform instrument and Agilent 7900. Reproducibility is better than ±4% (2 σ) for REE and better than ±6% (2 σ) for other elements (Supplementary Table 1).

Mineral major and trace element analyses by EPMA and LA-ICP-MS

Major element compositions of primary cumulus olivine, plagioclase and clinopyroxene were analyzed by electron probe microanalyzers (EPMAs) at Kanazawa University and the Geological survey of Japan, AIST. X-ray intensity map analyses were done with an EPMA at the Atmosphere and Ocean Research Institute, the University of Tokyo (Table 3). Trace element compositions (REEs, V, Cr, Co, Ni, Li, B, Sc, Rb, Sr, Y, Zr, Nb, Cs, Ba, Hf, Ta, Pb, Th and U) of clinopyroxene crystals were analyzed by laser ablation inductively coupled plasma mass spectrometry (LA-ICP-MS) at Kanazawa University. Three representative cumulus clinopyroxene crystals were chosen from each sample and three and two points in the core and rim of each crystal were analyzed for 13 samples of GT2A and for 9 samples of GT1A (Table-Supp).

The details of analytical conditions are provided in the supplementary information (Supplementary doc and Tables).

Table 2. Whole-rock compositions of core samples from GT1A and GT2A. Major elements (mass%) were analyzed by an X-ray fluorescence method using a ZSX primus II at the College of Science and Engineering, Kanazawa University, Ishikawa, Japan (Supplementary Table S1). Analytical procedures and errors are found in Supplementary materials and Kusano et al. (2014b) for the details. Whole-rock trace elements (µg/g) were analyzed at the Geological Survey of Japan by an inductively coupled plasma mass 108 spectrometry (ICP-MS) on a VG Platform instrument and Agilent 7900. Reproducibility is better than ±4% (2 σ) for REE and better than ±6% (2 σ) for other elements (see BHVO2 analysis in Table S1).

Hole_Core_Section_Interval	mbs		FeO*/MgO	Mg#	SiO_2	TiO_2	Al_2O_3	Fe_2O_3	MnO	MgO	CaO	Na_2O	K_2O	P_2O_5	Total
	Top	Bottom													
Hole GT1A															
GT1A_30_4_59-63	72.75	72.79	0.51	77.89	47.55	0.12	22.59	4.62	0.07	8.21	15.22	1.40	0.01	0.00	99.79
GT1A_30_4_63-67	72.79	72.83	0.42	80.90	49.90	0.37	11.48	5.70	0.11	12.18	18.64	0.79	0.02	0.01	99.21
GT1A_33_3_20-24	80.60	80.64	0.46	79.33	48.29	0.16	20.74	4.03	0.06	7.80	16.83	1.29	0.00	0.00	99.22
GT1A_38_1_52-56	91.67	91.71	0.37	82.96	47.22	0.22	12.76	6.45	0.11	15.84	15.88	0.56	0.01	0.00	99.05
GT1A_38_4_48-52	94.06	94.10	0.38	82.25	45.31	0.24	7.63	10.07	0.16	23.56	11.84	0.28	0.01	0.00	99.11
GT1A_41_3_33-37	99.34	99.38	0.41	81.32	44.25	0.19	7.36	11.37	0.17	25.00	10.59	0.26	0.01	0.00	99.20
GT1A_44_1_31-35	101.21	101.25	0.45	79.84	44.95	0.20	9.59	10.62	0.17	21.24	11.85	0.31	0.01	0.00	98.94
GT1A_45_2_43-47	104.72	104.76	0.49	78.59	47.39	0.21	18.50	5.47	0.09	10.14	16.21	1.11	0.02	0.00	99.14
GT1A_83_1_62-66	206.82	206.86	0.54	76.82	47.44	0.19	18.37	5.96	0.09	9.97	15.97	1.07	0.00	0.00	99.07
GT1A_83_4_20-24	208.46	208.50	0.48	78.63	47.52	0.23	17.05	5.92	0.09	10.99	16.35	0.93	0.01	0.01	99.09
GT1A_88_3_21-25	220.15	220.19	0.59	75.19	48.82	0.26	15.74	6.44	0.10	9.86	16.97	1.04	0.01	0.00	99.26
GT1A_95_2_38-42	237.17	237.21	0.55	76.56	48.66	0.27	18.01	5.43	0.09	8.96	16.73	1.25	0.01	0.00	99.41
GT1A_106_3_85-89	267.75	267.79	0.68	72.31	46.33	0.15	16.56	9.70	0.14	12.79	11.59	1.33	0.01	0.00	98.59
GT1A_122_3_11-15	309.14	309.18	0.42	80.77	48.58	0.20	17.57	4.70	0.08	9.96	17.04	1.06	0.01	0.00	99.20
GT1A_147_1_3-7	374.83	374.87	0.41	81.17	48.18	0.19	13.48	6.52	0.11	14.20	16.00	0.71	0.01	0.00	99.40
GT1A_152_4_13-17	392.47	392.51	0.38	82.47	47.65	0.20	13.88	6.26	0.10	14.86	15.64	0.67	0.01	0.00	99.26
GT1A_154_4_61-65	399.14	399.18	0.36	83.19	49.22	0.27	10.84	5.99	0.11	14.97	17.39	0.57	0.01	0.00	99.37
GT1A_156_1_53-57	402.78	402.82	0.41	81.12	47.95	0.20	16.30	5.50	0.09	11.93	16.24	0.81	0.01	0.00	99.02
Hole GT2A															
GT2A_20_3_55-59	44.47	44.51	0.61	74.49	49.08	0.35	16.93	6.06	0.11	8.93	15.96	1.72	0.04	0.01	99.18
GT2A_35_3_71-75	90.08	90.12	0.64	73.47	49.39	0.38	15.34	6.74	0.12	9.42	16.29	1.57	0.03	0.01	99.29
GT2A_46_3_56-60	120.30	120.34	0.64	73.55	48.52	0.45	19.95	9.26	0.16	13.00	16.61	0.90	0.01	0.01	99.35
GT2A_46_4_47-51	121.17	121.21	0.66	73.07	48.96	0.33	18.19	5.77	0.10	7.91	16.50	1.63	0.01	0.01	99.41
GT2A_50_1_47-51	130.75	130.79	0.71	71.50	47.53	0.15	22.54	5.89	0.08	7.46	13.68	1.87	0.02	0.01	99.23
GT2A_52_3_25-29	138.31	138.35	0.82	68.37	46.73	0.12	21.21	8.01	0.10	8.74	12.33	1.63	0.02	0.01	98.90
GT2A_75_3_8-12	196.52	196.56	0.63	73.79	46.59	0.17	16.51	9.14	0.13	13.00	12.31	1.40	0.02	0.01	99.28
GT2A_86_2_33-37	229.03	229.07	0.56	76.09	46.62	0.29	10.38	10.56	0.16	16.97	13.80	0.64	0.01	0.01	99.44
GT2A_102_1_3-7	273.88	273.92	0.51	77.82	47.20	0.18	16.08	7.23	0.11	12.81	14.91	0.72	0.02	0.00	99.26
GT2A_104_1_5-9	280.00	280.04	0.47	79.26	47.69	0.17	19.95	4.69	0.07	9.05	16.51	1.11	0.02	0.00	99.27
GT2A_104_4_53-57	282.73	282.77	0.49	78.33	47.60	0.26	15.06	7.14	0.11	13.02	15.00	0.91	0.03	0.01	99.12
GT2A_105_2_39-43	284.25	284.29	0.73	71.07	50.20	0.30	17.08	6.85	0.12	8.49	14.21	2.18	0.02	0.00	99.44
GT2A_117_2_6-10	314.34	314.38	0.65	73.31	47.11	0.30	15.90	8.12	0.13	11.26	15.40	1.04	0.01	0.01	99.28

Table 2. (Continued)

Hole_Core_Section_Interval	mbs		Cs	Rb	Ba	Th	U	Nb	Ta	La	Ce	Pb	Pr	Sr	Nd	Zr	Hf	Sm
	Top	Bottom																
Hole GT1A																		
GT1A_30_4_59-63	72.75	72.79	0.002	0.046	3.282	0.002	0.001	0.018	0.000	0.218	0.647	0.084	0.110	153.60	0.741	2.330	0.091	0.249
GT1A_30_4_63-67	72.79	72.83	0.004	0.187	2.756	0.020	0.008	0.168	0.011	0.372	1.443	0.077	0.303	76.59	1.956	14.498	0.472	0.924
GT1A_33_3_20-24	80.60	80.64	0.002	0.081	2.805	0.003	0.000	0.029	0.000	0.171	0.584	0.081	0.110	162.15	0.734	2.912	0.124	0.337
GT1A_38_1_52-56	91.67	91.71	0.004	0.087	2.439	0.003	0.001	0.039	0.000	0.172	0.653	0.072	0.129	99.33	0.954	4.296	0.182	0.420
GT1A_38_4_48-52	94.06	94.10	0.003	0.123	2.408	0.006	0.002	0.040	0.000	0.205	0.732	0.085	0.141	52.98	0.978	5.044	0.174	0.439
GT1A_41_3_33-37	99.34	99.38	0.001	0.047	1.238	0.002	0.001	0.026	0.000	0.113	0.437	0.046	0.092	53.23	0.652	3.001	0.115	0.338
GT1A_44_1_31-35	101.21	101.25	0.001	0.057	1.659	0.002	0.001	0.029	-0.001	0.125	0.455	0.051	0.103	66.02	0.672	2.816	0.128	0.326
GT1A_45_2_43-47	104.72	104.76	0.001	0.091	3.669	0.002	0.001	0.033	0.000	0.199	0.655	0.085	0.126	158.10	0.897	3.527	0.142	0.404
GT1A_83_1_62-66	206.82	206.86	0.002	0.057	2.898	0.002	0.001	0.025	-0.001	0.192	0.622	0.098	0.131	153.60	0.813	3.367	0.150	0.383
GT1A_83_4_20-24	208.46	208.50	0.001	0.036	2.995	0.003	0.001	0.035	0.000	0.202	0.727	0.104	0.149	141.89	0.950	4.581	0.188	0.467
GT1A_88_3_21-25	220.15	220.19	0.002	0.071	2.598	0.002	0.001	0.031	0.000	0.205	0.751	0.086	0.162	119.07	1.112	4.169	0.193	0.556
GT1A_95_2_38-42	237.17	237.21	0.011	0.268	6.698	0.027	0.008	0.243	0.012	0.429	1.176	0.161	0.221	142.96	1.368	5.968	0.233	0.645
GT1A_106_3_85-89	267.75	267.79	0.002	0.048	2.871	0.003	0.001	0.023	-0.001	0.157	0.487	0.028	0.093	118.18	0.618	2.052	0.097	0.291
GT1A_122_3_11-15	309.14	309.18	0.002	0.057	2.456	0.002	0.001	0.023	-0.001	0.197	0.681	0.062	0.138	106.62	0.947	3.263	0.147	0.404
GT1A_147_1_3-7	374.83	374.87	0.002	0.058	2.043	0.002	0.001	0.028	0.000	0.161	0.568	0.062	0.118	79.95	0.840	2.983	0.129	0.408
GT1A_152_4_13-17	392.47	392.51	0.002	0.046	2.148	0.002	0.001	0.016	-0.001	0.190	0.628	0.081	0.126	93.56	0.860	3.411	0.142	0.406
GT1A_154_4_61-65	399.14	399.18	0.003	0.123	2.541	0.007	0.002	0.058	0.002	0.231	0.822	0.085	0.171	67.52	1.180	4.916	0.204	0.606
GT1A_156_1_53-57	402.78	402.82	0.001	0.068	2.313	0.001	0.001	0.017	-0.001	0.201	0.650	0.080	0.126	107.11	0.860	3.195	0.136	0.398
Hole GT2A																		
GT2A_20_3_55-59	44.47	44.51	0.002	0.161	6.967	0.015	0.005	0.190	0.013	0.528	1.639	0.119	0.297	160.89	1.937	9.781	0.351	0.811
GT2A_35_3_71-75	90.08	90.12	0.001	0.132	4.955	0.006	0.002	0.075	0.005	0.348	1.223	0.095	0.251	157.44	1.694	7.541	0.305	0.858
GT2A_46_3_56-60	120.30	120.34	0.001	0.086	2.423	0.005	0.002	0.061	0.004	0.287	1.174	0.057	0.250	107.09	1.874	8.465	0.385	0.958
GT2A_46_4_47-51	121.17	121.21	0.001	0.097	4.870	0.006	0.003	0.077	0.006	0.346	1.148	0.101	0.223	181.98	1.497	6.678	0.276	0.689
GT2A_50_1_47-51	130.75	130.79	0.002	0.064	4.700	0.004	0.002	0.062	0.154	0.267	0.737	0.059	0.123	208.46	0.767	2.908	0.115	0.293
GT2A_52_3_25-29	138.31	138.35	0.002	0.077	4.451	0.003	0.001	0.041	0.003	0.238	0.645	0.087	0.104	200.59	0.622	2.105	0.081	0.230
GT2A_75_3_8-12	196.52	196.56	0.001	0.067	3.765	0.003	0.001	0.049	0.003	0.181	0.567	0.069	0.105	157.34	0.721	2.778	0.120	0.330
GT2A_86_2_33-37	229.03	229.07	0.001	0.056	1.962	0.003	0.001	0.053	0.003	0.197	0.760	0.043	0.166	80.32	1.126	4.841	0.201	0.525
GT2A_102_1_3-7	273.88	273.92	0.002	0.082	2.697	0.001	0.001	0.036	0.002	0.174	0.584	0.071	0.114	101.24	0.794	2.780	0.121	0.369
GT2A_104_1_5-9	280.00	280.04	0.002	0.050	3.824	0.004	0.001	0.071	0.006	0.246	0.746	0.078	0.132	146.47	0.858	3.068	0.121	0.378
GT2A_104_4_53-57	282.73	282.77	0.002	0.101	3.524	0.005	0.002	0.075	0.005	0.273	0.926	0.073	0.178	110.87	1.166	5.461	0.204	0.549
GT2A_105_2_39-43	284.25	284.29	0.001	0.061	4.697	0.001	0.000	0.034	0.002	0.211	0.726	0.040	0.140	155.36	0.981	3.658	0.169	0.497
GT2A_117_2_6-10	314.34	314.38	0.000	0.054	3.309	0.003	0.001	0.068	0.004	0.316	1.096	0.124	0.214	137.40	1.455	6.376	0.254	0.624

Table 2. (Continued)

Hole_Core_Section_Interval	mbs Top	mbs Bottom	Eu	Gd	Tb	Dy	Li	Ho	Y	Er	Tm	Yb	Lu	Be	V	Cr	Ni
Hole GT1A																	
GT1A_30_4_59-63	72.75	72.79	0.256	0.429	0.078	0.506	0.812	0.104	2.992	0.300	0.040	0.253	0.039	0.050	61.42	256.09	119.02
GT1A_30_4_63-67	72.79	72.83	0.387	1.429	0.269	1.836	1.624	0.391	10.913	1.054	0.160	0.934	0.141	0.048	228.05	780.66	149.41
GT1A_33_3_20-24	80.60	80.64	0.268	0.563	0.102	0.681	0.793	0.137	4.033	0.381	0.057	0.338	0.050	0.030	96.90	551.72	121.78
GT1A_38_1_52-56	91.67	91.71	0.245	0.714	0.132	0.871	0.932	0.193	5.313	0.501	0.071	0.443	0.066	0.025	133.33	1637.51	343.73
GT1A_38_4_48-52	94.06	94.10	0.222	0.740	0.136	0.898	1.199	0.196	5.403	0.544	0.075	0.491	0.069	0.030	127.53	1397.89	549.60
GT1A_41_3_33-37	99.34	99.38	0.167	0.524	0.100	0.661	1.178	0.141	4.045	0.404	0.056	0.356	0.049	0.016	109.78	1456.69	659.43
GT1A_44_1_31-35	101.21	101.25	0.183	0.566	0.104	0.701	0.992	0.149	4.217	0.418	0.058	0.385	0.055	0.024	110.70	1186.75	525.81
GT1A_45_2_43-47	104.72	104.76	0.266	0.654	0.129	0.848	0.881	0.183	5.024	0.507	0.068	0.436	0.063	0.044	131.06	193.40	138.66
GT1A_83_1_62-66	206.82	206.86	0.260	0.623	0.115	0.746	0.871	0.162	4.543	0.441	0.061	0.384	0.057	0.042	113.49	727.19	186.20
GT1A_83_4_20-24	208.46	208.50	0.285	0.718	0.135	0.866	0.553	0.192	5.217	0.515	0.071	0.447	0.067	0.042	139.91	705.37	175.50
GT1A_88_3_21-25	220.15	220.19	0.322	0.929	0.176	1.200	0.821	0.256	7.221	0.692	0.098	0.606	0.089	0.043	168.04	554.26	146.85
GT1A_95_2_38-42	237.17	237.21	0.366	0.968	0.184	1.179	0.821	0.261	7.197	0.693	0.100	0.620	0.086	0.058	169.63	284.50	104.72
GT1A_106_3_85-89	267.75	267.79	0.242	0.472	0.092	0.588	0.203	0.131	3.473	0.345	0.050	0.313	0.046	0.051	80.96	104.95	137.37
GT1A_122_3_11-15	309.14	309.18	0.277	0.734	0.137	0.893	0.304	0.197	5.530	0.526	0.076	0.474	0.070	0.042	128.24	159.60	146.85
GT1A_147_1_3-7	374.83	374.87	0.216	0.697	0.133	0.911	0.496	0.200	5.610	0.551	0.083	0.495	0.077	0.031	142.19	830.70	281.98
GT1A_152_4_13-17	392.47	392.51	0.236	0.662	0.125	0.816	0.834	0.180	5.038	0.499	0.073	0.426	0.066	0.035	133.78	888.21	256.21
GT1A_154_4_61-65	399.14	399.18	0.291	0.986	0.185	1.270	0.705	0.272	7.509	0.745	0.100	0.657	0.094	0.030	186.44	586.60	197.71
GT1A_156_1_53-57	402.78	402.82	0.260	0.681	0.130	0.852	0.351	0.182	5.097	0.510	0.071	0.439	0.064	0.040	123.11	986.76	257.10
Hole GT2A																	
GT2A_20_3_55-59	44.47	44.51	0.461	1.283	0.238	1.610	0.628	0.336	9.404	0.946	0.134	0.819	0.125	0.100	164.85	225.22	89.95
GT2A_35_3_71-75	90.08	90.12	0.440	1.293	0.251	1.668	0.748	0.359	9.925	1.009	0.145	0.876	0.135	0.072	203.08	90.02	61.15
GT2A_46_3_56-60	120.30	120.34	0.440	1.574	0.292	2.013	0.835	0.431	11.794	1.179	0.167	1.034	0.147	0.050	253.77	107.25	90.95
GT2A_46_4_47-51	121.17	121.21	0.397	1.099	0.208	1.386	0.584	0.290	8.052	0.824	0.114	0.704	0.103	0.079	171.54	69.14	55.37
GT2A_50_1_47-51	130.75	130.79	0.291	0.426	0.085	0.562	0.458	0.116	3.264	0.333	0.042	0.287	0.045	0.076	65.99	24.67	54.11
GT2A_52_3_25-29	138.31	138.35	0.265	0.349	0.061	0.397	0.347	0.086	2.322	0.227	0.035	0.218	0.031	0.067	48.57	21.02	89.01
GT2A_75_3_8-12	196.52	196.56	0.240	0.532	0.094	0.634	0.654	0.136	3.664	0.378	0.054	0.351	0.049	0.057	88.79	54.27	100.81
GT2A_86_2_33-37	229.03	229.07	0.260	0.881	0.168	1.154	0.638	0.243	6.732	0.670	0.093	0.600	0.091	0.037	153.21	184.88	197.75
GT2A_102_1_3-7	273.88	273.92	0.247	0.608	0.110	0.749	1.958	0.167	4.464	0.452	0.062	0.390	0.057	0.032	103.35	294.03	294.03
GT2A_104_1_5-9	280.00	280.04	0.272	0.616	0.116	0.741	0.667	0.158	4.303	0.429	0.062	0.379	0.056	0.054	88.15	584.06	140.92
GT2A_104_4_53-57	282.73	282.77	0.298	0.877	0.154	1.051	1.017	0.227	6.285	0.617	0.094	0.544	0.082	0.056	98.15	342.76	268.94
GT2A_105_2_39-43	284.25	284.29	0.353	0.871	0.167	1.155	0.408	0.251	6.732	0.680	0.099	0.621	0.093	0.064	130.96	333.57	104.79
GT2A_117_2_6-10	314.34	314.38	0.372	1.033	0.191	1.272	1.285	0.277	7.513	0.750	0.106	0.669	0.101	0.065	147.10	543.78	142.10

Table 3a. Average core and rim compositions (mass%) of olivine. n is the number of analyses averaged.

Hole_Core_Section_Interval	n		Fo	SiO$_2$	TiO$_2$	Al$_2$O$_3$	FeO	MnO	MgO	CaO	NiO	Total
GT1A												
GT1A_30_4_59-63	12	Core average	78.14	39.23	0.02	0.00	20.27	0.32	40.64	0.04	0.08	100.60
		1σ	0.75	0.32	0.02	0.01	0.45	0.06	0.43	0.02	0.03	
	12	Rim average	78.46	39.23	0.01	0.01	19.99	0.29	40.84	0.03	0.06	100.47
		1σ	0.71	0.35	0.02	0.01	0.30	0.04	0.44	0.01	0.03	
GT1A_45_2_43-47	12	Core average	79.55	39.74	0.01	0.00	19.28	0.27	42.09	0.05	0.08	101.52
		1σ	0.52	0.11	0.02	0.01	0.35	0.04	0.28	0.01	0.03	
	12	Rim average	79.57	39.77	0.01	0.01	19.26	0.28	42.08	0.05	0.09	101.56
		1σ	0.52	0.11	0.02	0.01	0.35	0.04	0.28	0.01	0.03	
GT1A_83_1_62-66	9	Core average	78.94	39.61	0.02	0.00	19.74	0.29	41.51	0.05	0.09	101.32
		1σ	0.43	0.10	0.02	0.01	0.35	0.05	0.21	0.02	0.04	
	9	Rim average	77.58	39.36	0.01	0.00	20.85	0.31	40.48	0.05	0.08	101.14
		1σ	1.32	0.18	0.01	0.01	0.97	0.05	0.70	0.02	0.03	
GT1A_95_2_38-42	9	Core average	76.23	39.21	0.01	0.01	22.14	0.33	39.84	0.03	0.09	101.65
		1σ	0.30	0.13	0.01	0.01	0.18	0.05	0.18	0.02	0.03	
	9	Rim average	76.18	39.24	0.00	0.01	22.14	0.30	39.73	0.04	0.07	101.54
		1σ	0.58	0.20	0.01	0.01	0.34	0.03	0.35	0.02	0.03	
GT1A_152_4_13-17	9	Core average	82.52	39.89	0.01	0.01	16.72	0.25	44.29	0.05	0.12	101.34
		1σ	0.33	0.23	0.02	0.01	0.19	0.06	0.19	0.02	0.03	
	9	Rim average	82.26	39.89	0.02	0.01	16.99	0.23	44.18	0.03	0.10	101.45
		1σ	0.65	0.18	0.03	0.01	0.35	0.05	0.38	0.01	0.04	
GT2A												
GT2A_46_3_56-60	9	Core average	73.25	38.95	0.13	0.01	25.07	3.32	38.51	0.03	0.05	106.08
		1σ	0.52	0.38	0.37	0.02	0.34	1.35	0.32	0.01	0.03	
	3	Rim average	73.36	39.11	0.00	0.02	24.97	4.28	38.57	0.03	0.07	107.05
		1σ	0.38	0.42	0.01	0.02	0.19	1.67	0.25	0.01	0.05	
GT2A_46_4_47-51	9	Core average	73.37	38.96	0.02	0.00	24.97	0.39	38.59	0.05	0.04	103.03
		1σ	0.32	0.26	0.02	0.01	0.21	0.02	0.20	0.01	0.03	
	4	Rim average	73.25	39.10	0.02	0.02	25.09	0.38	38.55	0.04	0.04	103.24
		1σ	0.42	0.37	0.01	0.03	0.33	0.04	0.24	0.01	0.02	
GT2A_50_1_47-51	9	Core average	73.87	39.18	0.01	0.02	24.44	0.38	38.77	0.04	0.04	102.88
		1σ	0.38	0.27	0.01	0.02	0.33	0.02	0.20	0.01	0.03	
	4	Rim average	74.01	39.47	0.01	0.01	24.21	0.40	38.68	0.03	0.04	102.85
		1σ	0.47	0.50	0.01	0.02	0.38	0.04	0.26	0.01	0.03	
GT2A_52_3_25-29	9	Core average	73.28	37.76	0.01	0.02	24.84	0.39	38.22	0.05	0.05	101.33
		1σ	0.27	0.22	0.01	0.02	0.21	0.03	0.15	0.01	0.03	
	6	Rim average	73.47	37.82	0.02	0.02	24.57	0.41	38.17	0.05	0.03	101.08
		1σ	0.36	0.63	0.02	0.03	0.19	0.05	0.23	0.01	0.02	
GT2A_75_3_8-12	9	Core average	75.62	39.49	0.01	0.01	22.97	0.34	39.98	0.05	0.03	102.86
		1σ	0.32	0.14	0.01	0.01	0.19	0.04	0.20	0.01	0.03	
	6	Rim average	75.72	39.57	0.01	0.01	22.86	0.33	39.98	0.04	0.05	102.86
		1σ	0.43	0.33	0.01	0.01	0.36	0.03	0.22	0.01	0.04	
GT2A_104_1_5-9	9	Core average	79.84	39.13	0.02	0.01	19.21	0.28	42.68	0.04	0.12	101.49
		1σ	0.38	0.29	0.01	0.02	0.21	0.02	0.22	0.01	0.03	
	6	Rim average	79.97	38.92	0.01	0.02	19.03	0.28	42.61	0.06	0.08	101.01
		1σ	0.37	0.21	0.01	0.02	0.25	0.03	0.20	0.01	0.04	
GT2A_105_2_39-43	10	Core average	72.74	38.41	0.01	0.02	25.36	0.40	37.97	0.05	0.07	102.29
		1σ	0.25	0.27	0.01	0.02	0.24	0.04	0.11	0.01	0.02	
	6	Rim average	72.83	38.52	0.01	0.02	25.17	0.38	37.85	0.05	0.06	102.06
		1σ	0.22	0.17	0.00	0.02	0.25	0.05	0.07	0.01	0.03	
GT2A_117_2_6-10	9	Core average	74.59	39.16	0.00	0.01	23.72	0.40	39.06	0.04	0.06	102.45
		1σ	0.49	0.34	0.01	0.01	0.45	0.03	0.23	0.01	0.02	
	6	Rim average	74.69	39.31	0.01	0.01	23.56	0.36	39.00	0.04	0.07	102.36
		1σ	0.52	0.34	0.01	0.02	0.44	0.04	0.27	0.01	0.04	

The magmatic conditions and hypersolidus deformation of lower crustal magma chamber below a fast-spreading ridge — Insight from the core analyses of the Oman ICDP drill holes GT1A & GT2A

Table 3b. Average core and rim compositions (mass%) of plagioclase. n is the number of analyses averaged.

Hole_Core_Section_Interval	n		An	Ab	Or	SiO$_2$	TiO$_2$	Al$_2$O$_3$	FeO	MnO	MgO	CaO	Na$_2$O	K$_2$O	Total
GT1A															
GT1A_30_4_59-63	6	Cumulus core average	81.61	18.25	0.14	47.45	0.04	32.33	0.45	0.02	0.04	16.35	2.02	0.02	98.71
		1σ	5.07	3.63	0.03	0.97	0.02	0.59	0.04	0.02	0.02	0.65	0.39	0.01	
	7	Cumulus rim average	80.37	19.52	0.10	47.65	0.02	32.18	0.51	0.02	0.03	16.16	2.17	0.02	98.75
		1σ	0.83	0.53	0.02	0.20	0.02	0.21	0.11	0.03	0.02	0.11	0.06	0.01	
	9	Neoblast core average	80.04	19.88	0.08	47.84	0.02	32.12	0.47	0.01	0.05	16.08	2.21	0.01	98.82
		1σ	0.88	0.55	0.02	0.26	0.02	0.18	0.05	0.02	0.02	0.12	0.06	0.01	
	9	Neoblast rim average	80.94	19.00	0.05	47.53	0.02	32.33	0.48	0.02	0.04	16.17	2.10	0.01	98.70
		1σ	1.49	1.15	0.01	0.45	0.03	0.16	0.08	0.01	0.01	0.18	0.12	0.01	
GT1A_45_2_43-47	9	Cumulus core average	80.11	19.80	0.09	48.25	0.02	32.27	0.49	0.02	0.05	16.59	2.27	0.02	99.97
		1σ	2.22	1.58	0.02	0.46	0.02	0.18	0.04	0.02	0.03	0.30	0.17	0.01	
	9	Cumulus rim average	81.22	18.72	0.06	47.91	0.03	32.59	0.52	0.02	0.03	16.87	2.15	0.01	100.13
		1σ	0.81	0.56	0.02	0.18	0.02	0.23	0.06	0.02	0.01	0.11	0.06	0.01	
	9	Neoblast core average	81.01	18.89	0.10	47.88	0.02	32.33	0.47	0.01	0.04	16.74	2.16	0.02	99.66
		1σ	0.74	0.46	0.02	0.12	0.01	0.16	0.05	0.01	0.02	0.10	0.05	0.01	
	9	Neoblast rim average	81.92	18.03	0.05	47.76	0.02	32.46	0.54	0.01	0.04	16.96	2.06	0.01	99.85
		1σ	1.32	0.88	0.01	0.25	0.03	0.31	0.05	0.01	0.03	0.18	0.10	0.01	
GT1A_83_1_62-66	9	Cumulus core average	80.23	19.67	0.10	48.10	0.02	32.76	0.46	0.01	0.06	16.45	2.23	0.02	100.11
		1σ	1.49	0.68	0.02	0.18	0.02	0.12	0.06	0.01	0.06	0.22	0.07	0.01	
	9	Cumulus rim average	81.31	18.62	0.07	47.76	0.03	33.02	0.50	0.01	0.03	16.53	2.09	0.01	99.98
		1σ	1.47	1.04	0.03	0.25	0.02	0.23	0.10	0.02	0.01	0.19	0.11	0.01	
	9	Neoblast core average	80.33	19.62	0.05	47.93	0.02	32.77	0.46	0.01	0.04	16.32	2.20	0.01	99.76
		1σ	0.80	0.54	0.01	0.16	0.02	0.08	0.03	0.02	0.01	0.11	0.06	0.01	
	9	Neoblast rim average	82.33	17.59	0.08	47.46	0.02	33.17	0.51	0.01	0.04	16.67	1.97	0.01	99.87
		1σ	4.29	3.41	0.02	0.72	0.02	0.60	0.13	0.02	0.04	0.51	0.37	0.01	
GT1A_95_2_38-42	9	Cumulus core average	77.23	22.65	0.12	48.30	0.03	31.22	0.61	0.01	0.29	15.52	2.52	0.02	98.52
		1σ	3.71	2.57	0.02	0.76	0.02	0.43	0.24	0.02	0.71	0.51	0.27	0.01	
	9	Cumulus rim average	81.11	18.80	0.09	47.44	0.03	31.83	0.83	0.02	0.34	16.23	2.08	0.02	98.81
		1σ	5.66	2.74	0.02	0.96	0.02	0.68	0.38	0.02	0.53	0.82	0.29	0.01	
	9	Neoblast core average	79.14	20.78	0.07	47.77	0.03	31.73	0.51	0.03	0.03	16.14	2.34	0.01	98.61
		1σ	0.68	0.38	0.02	0.32	0.02	0.06	0.06	0.03	0.01	0.10	0.04	0.01	
	9	Neoblast rim average	80.32	19.60	0.08	47.61	0.02	31.93	0.54	0.04	0.18	16.31	2.20	0.01	98.84
		1σ	3.08	2.16	0.02	0.62	0.03	0.38	0.17	0.03	0.33	0.41	0.23	0.01	
GT1A_152_4_13-17	9	Cumulus core average	83.96	15.96	0.07	46.94	0.02	32.53	0.38	0.01	0.04	16.98	1.78	0.01	98.69
		1σ	1.22	0.60	0.02	0.35	0.02	0.29	0.04	0.01	0.02	0.17	0.06	0.01	
	9	Cumulus rim average	85.32	14.59	0.08	46.67	0.02	32.52	0.61	0.01	0.26	17.01	1.61	0.01	98.73
		1σ	2.54	1.08	0.02	0.60	0.01	0.46	0.31	0.02	0.38	0.36	0.11	0.01	
	9	Neoblast core average	84.01	15.92	0.07	47.39	0.03	32.43	0.38	0.02	0.03	17.02	1.78	0.01	99.09
		1σ	0.96	0.75	0.01	0.26	0.03	0.18	0.04	0.02	0.01	0.11	0.08	0.00	
	9	Neoblast rim average	84.65	15.29	0.07	47.20	0.01	32.44	0.40	0.01	0.04	17.19	1.72	0.01	99.02
		1σ	1.17	0.80	0.02	0.22	0.02	0.23	0.08	0.01	0.01	0.15	0.09	0.01	

Table 3b. (Continued)

Hole_Core_Section_Interval	n		An	Ab	Or	SiO_2	TiO_2	Al_2O_3	FeO	MnO	MgO	CaO	Na_2O	K_2O	Total
GT2A															
GT2A_35_3_71-75	9	Cumulus core average	70.16	29.63	0.21	51.10	0.03	31.14	0.44	0.01	0.03	14.50	3.39	0.04	100.68
		1σ	3.10	2.60	0.02	0.55	0.01	0.34	0.04	0.01	0.01	0.44	0.28	0.01	
	6	Cumulus rim average	71.17	28.66	0.17	50.75	0.02	31.20	0.45	0.01	0.03	14.67	3.27	0.03	100.42
		1σ	1.19	0.82	0.02	0.35	0.02	0.30	0.03	0.01	0.01	0.18	0.09	0.01	
GT2A_46_3_56-60	9	Cumulus core average	75.31	24.54	0.16	50.45	0.04	31.92	0.44	0.31	0.04	15.43	2.78	0.03	101.43
		1σ	0.89	0.61	0.01	0.26	0.01	0.16	0.03	0.62	0.02	0.13	0.07	0.01	
	3	Cumulus rim average	74.49	25.34	0.17	50.94	0.02	32.02	0.46	0.77	0.03	15.28	2.87	0.03	102.42
		1σ	0.23	0.30	0.01	0.17	0.01	0.06	0.06	0.58	0.01	0.01	0.03	0.01	
GT2A_104_4_53-57	6	Cumulus core average	77.61	22.26	0.13	48.59	0.04	31.70	0.43	0.25	0.04	15.88	2.52	0.02	99.46
		1σ	3.34	2.60	0.03	0.64	0.01	0.52	0.04	0.60	0.04	0.44	0.28	0.01	
	2	Cumulus rim average	80.03	19.86	0.12	47.77	0.02	32.54	0.42	1.07	0.02	16.31	2.24	0.02	100.40
		1σ	2.93	2.23	0.04	0.23	0.01	0.26	0.05	1.52	0.01	0.38	0.24	0.02	
GT2A_20_3_55-59	9	Cumulus core average	73.39	26.34	0.27	50.42	0.05	31.68	0.48	0.01	0.03	15.20	3.01	0.05	100.92
		1σ	3.01	2.40	0.02	0.37	0.02	0.33	0.03	0.01	0.01	0.42	0.26	0.01	
	6	Cumulus rim average	71.95	27.83	0.23	50.80	0.04	31.40	0.46	0.00	0.03	14.90	3.19	0.04	100.87
		1σ	3.84	3.10	0.02	0.54	0.01	0.54	0.04	0.01	0.01	0.54	0.33	0.01	
GT2A_46_4_47-51	9	Cumulus core average	74.74	25.01	0.24	50.26	0.03	31.97	0.49	0.01	0.03	15.49	2.87	0.04	101.19
		1σ	1.43	1.15	0.01	0.32	0.01	0.27	0.02	0.01	0.01	0.20	0.13	0.01	
	6	Cumulus rim average	73.59	26.18	0.23	50.26	0.03	31.82	0.46	0.01	0.03	15.23	2.99	0.04	100.88
		1σ	1.34	0.91	0.01	0.39	0.01	0.30	0.07	0.02	0.01	0.20	0.10	0.01	
GT2A_50_1_47-51	9	Cumulus core average	74.25	25.60	0.15	49.79	0.03	31.82	0.46	0.01	0.03	15.34	2.92	0.03	100.42
		1σ	1.10	1.02	0.02	0.34	0.02	0.14	0.05	0.01	0.01	0.14	0.11	0.01	
	6	Cumulus rim average	74.23	25.64	0.13	49.85	0.02	31.79	0.48	0.00	0.03	15.32	2.92	0.02	100.45
		1σ	0.95	0.83	0.01	0.44	0.01	0.17	0.04	0.01	0.01	0.12	0.09	0.01	
GT2A_52_3_25-29	9	Cumulus core average	74.11	25.70	0.19	48.66	0.04	31.74	0.46	0.01	0.03	15.06	2.89	0.03	98.93
		1σ	3.54	1.50	0.06	1.23	0.02	0.29	0.06	0.02	0.03	0.56	0.14	0.03	
	6	Cumulus rim average	75.67	24.21	0.12	48.81	0.03	31.89	0.51	0.01	0.03	15.52	2.74	0.02	99.57
		1σ	4.12	3.16	0.02	0.77	0.02	0.51	0.07	0.01	0.00	0.84	0.34	0.01	
GT2A_75_3_8-12	9	Cumulus core average	71.61	28.22	0.17	50.70	0.04	31.47	0.45	0.01	0.01	14.84	3.23	0.03	100.81
		1σ	6.96	5.64	0.02	1.48	0.02	0.82	0.03	0.02	0.01	0.99	0.60	0.01	
	6	Cumulus rim average	73.62	26.26	0.12	50.18	0.03	31.91	0.48	0.01	0.04	15.28	3.01	0.02	100.96
		1σ	2.34	1.64	0.02	0.57	0.01	0.44	0.08	0.01	0.01	0.34	0.18	0.01	
GT2A_86_2_33-37	9	Cumulus core average	80.13	19.73	0.14	47.22	0.03	32.59	0.48	0.01	0.03	16.33	2.22	0.02	98.94
		1σ	1.12	0.61	0.01	0.63	0.02	0.12	0.07	0.02	0.01	0.16	0.07	0.00	
	6	Cumulus rim average	79.55	20.32	0.13	47.70	0.03	32.59	0.45	0.01	0.03	16.27	2.30	0.02	99.39
		1σ	0.94	0.82	0.01	0.41	0.01	0.26	0.03	0.01	0.01	0.11	0.09	0.01	
GT2A_102_1_3-7	9	Cumulus core average	83.87	16.05	0.09	46.18	0.03	33.33	0.42	0.02	0.03	17.00	1.80	0.01	98.81
		1σ	1.60	0.95	0.01	0.46	0.01	0.18	0.03	0.02	0.01	0.22	0.10	0.00	
	6	Cumulus rim average	83.90	16.01	0.09	46.24	0.02	33.21	0.44	0.01	0.03	17.03	1.80	0.02	98.79
		1σ	2.55	1.91	0.02	0.40	0.01	0.32	0.07	0.01	0.01	0.31	0.21	0.01	
GT2A_104_1_5-9	9	Cumulus core average	82.34	17.53	0.13	46.18	0.03	32.93	0.44	0.01	0.03	16.76	1.97	0.02	98.37
		1σ	0.93	0.65	0.02	0.29	0.01	0.28	0.04	0.01	0.01	0.12	0.07	0.01	
	6	Cumulus rim average	82.46	17.44	0.10	46.26	0.03	33.01	0.44	0.03	0.03	16.76	1.96	0.02	98.52
		1σ	1.39	1.04	0.01	0.33	0.02	0.11	0.03	0.02	0.02	0.17	0.11	0.01	
GT2A_105_2_39-43	9	Cumulus core average	62.81	36.98	0.21	52.13	0.05	29.56	0.37	0.01	0.04	13.02	4.24	0.04	99.46
		1σ	2.24	2.05	0.02	0.54	0.02	0.36	0.03	0.02	0.01	0.34	0.21	0.01	
	6	Cumulus rim average	66.13	33.69	0.18	51.04	0.02	30.31	0.40	0.02	0.03	13.76	3.87	0.03	99.48
		1σ	3.78	2.82	0.03	0.73	0.02	0.53	0.07	0.01	0.01	0.59	0.29	0.01	
GT2A_117_2_6-10	9	Cumulus core average	80.30	19.59	0.10	48.51	0.02	32.85	0.44	0.02	0.03	16.48	2.22	0.02	100.59
		1σ	1.54	0.96	0.02	0.36	0.01	0.22	0.03	0.01	0.01	0.22	0.10	0.01	
	6	Cumulus rim average	79.42	20.45	0.13	48.75	0.02	32.87	0.47	0.01	0.03	16.22	2.31	0.02	100.71
		1σ	1.03	0.57	0.02	0.16	0.02	0.11	0.06	0.01	0.01	0.15	0.06	0.01	

Table 3c. Average core and rim compositions of clinopyroxene and compositions of clinopyroxene core with the maximum Mg# in each sample. n is the number of analyses averaged and out of which the maximum Mg#s of clinopyroxene are chosen.

Hole_Core_Section_Interval	n		Mg#	Wo	En	Fs	SiO$_2$	TiO$_2$	Al$_2$O$_3$	FeO	MnO	MgO	CaO	Na$_2$O	K$_2$O	Cr$_2$O$_3$	NiO	Total
GT1A																		
GT1A_30_4_59-63	15	Core average	83.89	44.33	46.70	8.97	52.69	0.42	2.61	5.57	0.14	16.28	21.50	0.32	0.01	0.26	0.02	99.81
		1σ	1.83	0.97	1.30	0.50	0.34	0.08	0.16	0.30	0.03	0.39	0.36	0.05	0.02	0.10	0.02	
	15	Rim average	82.23	44.23	45.85	9.91	52.25	0.75	2.54	6.15	0.18	15.96	21.42	0.33	0.00	0.17	0.01	99.76
		1σ	1.42	1.29	1.11	0.42	0.29	0.08	0.11	0.24	0.04	0.30	0.54	0.02	0.01	0.09	0.02	
	15	Core max Mg#	85.50	44.68	47.30	8.02	52.83	0.24	2.60	5.01	0.14	16.56	21.76	0.33	0.00	0.44	0.06	99.97
GT1A_30_4_63-67	12	Core average	84.72	43.81	47.61	8.58	52.64	0.40	2.57	5.37	0.15	16.71	21.39	0.25	0.00	0.19	0.03	99.70
		1σ	2.91	2.17	2.09	1.01	0.54	0.13	0.39	0.61	0.03	0.58	0.89	0.04	0.00	0.05	0.03	
	12	Rim average	81.32	44.31	45.29	10.40	51.95	0.77	2.45	6.44	0.17	15.73	21.41	0.35	0.01	0.14	0.01	99.41
		1σ	1.53	1.47	1.13	0.64	0.42	0.11	0.28	0.38	0.04	0.29	0.62	0.05	0.01	0.05	0.02	
	12	Core max Mg#	86.53	44.30	48.19	7.50	52.80	0.27	2.69	4.71	0.17	16.98	21.72	0.19	0.01	0.29	0.00	99.85
GT1A_33_3_20-24	15	Core average	82.59	44.18	46.10	9.72	53.22	0.46	2.67	6.27	0.18	16.70	22.27	0.23	0.01	0.27	0.07	102.33
		1σ	4.39	1.61	1.68	0.35	1.72	0.10	0.32	0.68	0.09	1.00	1.07	0.03	0.02	0.15	0.10	
	15	Rim average	81.69	45.35	44.64	10.01	53.14	0.59	2.47	6.44	0.20	16.11	22.77	0.26	0.01	0.25	0.08	102.23
		1σ	2.10	0.89	0.88	0.20	1.26	0.07	0.27	0.37	0.07	0.46	0.68	0.05	0.02	0.17	0.08	
	15	Core max Mg#	83.73	45.28	45.82	8.90	54.11	0.51	2.77	5.83	0.12	16.83	23.14	0.26	0.00	0.27	0.04	103.88
GT1A_38_1_52-56	15	Core average	87.34	45.64	47.48	6.88	52.81	0.38	3.01	4.34	0.11	16.80	22.47	0.26	0.00	0.54	0.02	100.74
		1σ	0.97	0.53	0.60	0.37	0.32	0.06	0.20	0.23	0.03	0.17	0.21	0.03	0.00	0.11	0.03	
	15	Rim average	85.89	45.36	46.93	7.71	52.67	0.55	2.78	4.84	0.13	16.52	22.22	0.30	0.00	0.52	0.01	100.54
		1σ	1.29	1.11	0.96	0.32	0.33	0.04	0.14	0.19	0.04	0.27	0.47	0.02	0.01	0.06	0.02	
	15	Core max Mg#	88.59	46.03	47.81	6.16	52.85	0.38	3.04	3.87	0.12	16.86	22.58	0.22	0.01	0.61	0.10	100.64
GT1A_38_4_48-52	15	Core average	87.21	45.87	47.21	6.92	51.83	0.42	3.06	4.30	0.11	16.44	22.23	0.27	0.00	0.63	0.02	99.30
		1σ	0.94	0.65	0.62	0.33	0.29	0.07	0.15	0.20	0.04	0.17	0.26	0.03	0.00	0.10	0.02	
	15	Rim average	85.25	45.49	46.47	8.04	51.79	0.72	2.78	4.97	0.14	16.11	21.95	0.37	0.01	0.58	0.02	99.43
		1σ	1.11	0.53	0.78	0.20	0.36	0.09	0.11	0.11	0.03	0.24	0.19	0.03	0.01	0.05	0.02	
	15	Core max Mg#	88.06	45.06	48.39	6.56	51.85	0.44	2.95	4.06	0.12	16.78	21.74	0.25	0.00	0.59	0.01	98.78
GT1A_41_3_33-37	15	Core average	85.97	45.43	46.91	7.66	51.98	0.46	3.27	4.80	0.12	16.50	22.23	0.27	0.00	0.55	0.04	100.21
		1σ	1.75	1.11	1.13	0.66	0.36	0.10	0.27	0.41	0.04	0.32	0.44	0.02	0.00	0.18	0.02	
	15	Rim average	85.13	45.82	46.12	8.06	51.82	0.56	3.03	5.03	0.15	16.15	22.33	0.31	0.00	0.69	0.02	100.09
		1σ	1.10	0.65	0.76	0.28	0.48	0.04	0.11	0.17	0.03	0.23	0.25	0.02	0.01	0.10	0.03	
	15	Core max Mg#	87.17	47.35	45.90	6.75	51.90	0.38	3.09	4.23	0.07	16.11	23.13	0.28	0.01	0.48	0.07	99.74
GT1A_44_1_31-35	9	Core average	83.93	45.28	45.92	8.80	51.42	0.56	3.09	5.50	0.16	16.10	22.09	0.29	0.01	0.60	0.12	99.93
		1σ	2.45	2.16	1.74	0.91	0.46	0.10	0.28	0.55	0.08	0.47	0.91	0.04	0.02	0.23	0.09	
	5	Rim average	83.69	45.96	45.23	8.81	51.29	0.70	3.04	5.49	0.24	15.80	22.33	0.28	0.02	0.69	0.00	99.86
		1σ	0.59	0.66	0.36	0.34	0.24	0.13	0.11	0.21	0.05	0.06	0.28	0.04	0.02	0.09	0.08	
	9	Core max Mg#	85.37	46.07	46.04	7.89	51.71	0.42	2.94	4.95	0.13	16.21	22.57	0.22	0.00	0.62	0.23	100.00
GT1A_45_2_43-47	15	Core average	81.88	43.74	46.06	10.19	52.25	0.67	2.84	6.41	0.16	16.24	21.46	0.34	0.01	0.07	0.02	100.46
		1σ	2.11	1.78	1.67	0.53	0.25	0.05	0.23	0.30	0.04	0.48	0.75	0.04	0.01	0.06	0.02	
	15	Rim average	83.20	44.80	45.93	9.27	52.35	0.59	2.68	5.83	0.16	16.21	22.01	0.32	0.00	0.09	0.02	100.27
		1σ	1.33	1.19	0.99	0.43	0.34	0.04	0.29	0.26	0.04	0.27	0.50	0.04	0.00	0.04	0.02	
		Core max Mg#	82.66	45.86	44.76	9.39	52.20	0.75	3.14	5.84	0.10	15.63	22.28	0.39	0.00	0.14	0.00	100.47
GT1A_83_1_62-56	15	Core average	81.70	43.93	45.81	10.26	51.86	0.57	3.23	6.37	0.16	15.95	21.28	0.35	0.01	0.45	0.02	100.25
		1σ	3.13	2.51	2.46	0.76	0.44	0.05	0.42	0.43	0.03	0.71	1.03	0.03	0.01	0.11	0.02	
	15	Rim average	82.72	44.30	46.07	9.62	52.36	0.54	2.65	6.03	0.18	16.20	21.68	0.33	0.00	0.31	0.02	100.31
		1σ	0.82	0.52	0.56	0.32	0.26	0.05	0.20	0.19	0.03	0.16	0.21	0.03	0.01	0.05	0.03	
	15	Core max Mg#	82.66	44.73	45.69	9.59	52.11	0.66	2.86	5.99	0.17	16.02	21.82	0.37	0.00	0.32	0.00	100.31
GT1A_83_4_20-24	9	Core average	81.51	45.16	44.70	10.14	50.68	0.62	2.93	6.23	0.17	15.40	21.64	0.26	0.01	0.38	0.06	98.37
		1σ	1.56	0.60	0.59	0.13	0.42	0.09	0.29	0.23	0.06	0.34	0.38	0.04	0.01	0.14	0.08	
	5	Rim average	81.43	45.24	44.59	10.17	50.94	0.59	2.74	6.26	0.19	15.39	21.72	0.26	0.02	0.34	0.08	98.51
		1σ	0.94	0.37	0.37	0.08	0.19	0.08	0.05	0.24	0.15	0.17	0.25	0.02	0.03	0.12	0.13	
	9	Core max Mg#	82.24	46.08	44.34	9.58	50.96	0.68	2.81	5.81	0.18	15.09	21.82	0.32	0.01	0.38	0.00	98.06
GT1A_88_3_21-25	9	Core average	79.23	43.11	45.07	11.81	51.80	0.57	2.50	7.41	0.17	15.86	21.11	0.27	0.02	0.26	0.05	100.02
		1σ	3.46	3.24	2.78	1.23	0.46	0.12	0.29	0.72	0.10	0.77	1.38	0.05	0.02	0.12	0.04	
	9	Rim average	80.49	44.91	44.34	10.75	51.48	0.65	2.55	6.69	0.18	15.49	21.83	0.29	0.00	0.21	0.04	99.42
		1σ	1.40	1.08	0.98	0.56	0.52	0.10	0.20	0.34	0.06	0.28	0.44	0.03	0.01	0.07	0.05	
	9	Core max Mg#	80.20	45.46	43.75	10.80	51.33	0.63	2.35	6.74	0.19	15.32	22.15	0.26	0.02	0.42	0.03	99.44
GT1A_95_2_38-42	13	Core average	80.14	43.31	45.43	11.26	52.43	0.65	2.65	7.02	0.19	15.90	21.09	0.36	0.00	0.09	0.02	100.40
		1σ	2.53	1.94	1.99	0.72	0.23	0.09	0.12	0.42	0.04	0.58	0.80	0.04	0.00	0.06	0.02	
	15	Rim average	80.90	43.67	45.57	10.76	52.44	0.64	2.50	6.72	0.20	15.97	21.30	0.35	0.01	0.12	0.02	100.27
		1σ	1.36	1.10	1.03	0.46	0.27	0.04	0.13	0.27	0.03	0.29	0.46	0.03	0.01	0.03	0.03	
	15	Core max Mg#	81.28	44.78	44.88	10.34	52.11	0.64	2.61	6.41	0.27	15.61	21.67	0.35	0.00	0.10	0.00	99.77

Table 3c. (Continued)

Hole_Core_Section_Interval	n		Mg#	Wo	En	Fs	SiO₂	TiO₂	Al₂O₃	FeO	MnO	MgO	CaO	Na₂O	K₂O	Cr₂O₃	NiO	Total
GT1A_106_3_85-89	8	Core average	77.10	43.61	43.48	12.91	51.24	0.73	2.61	8.04	0.17	15.18	21.18	0.31	0.00	0.09	0.08	99.61
		1σ	1.90	1.87	1.42	0.92	0.33	0.10	0.19	0.55	0.10	0.38	0.79	0.04	0.02	0.08	0.09	
	9	Rim average	78.14	44.19	43.61	12.20	51.48	0.67	2.46	7.62	0.22	15.28	21.54	0.30	0.01	0.11	0.05	99.75
		1σ	1.76	1.68	1.34	0.74	0.24	0.11	0.10	0.44	0.12	0.37	0.71	0.06	0.01	0.07	0.06	
	8	Core max Mg#	78.49	44.78	43.34	11.88	51.23	0.76	2.64	7.42	0.09	15.19	21.84	0.26	0.00	0.10	0.08	99.61
GT1A_122_3_11-15	12	Core average	83.14	44.71	45.97	9.32	51.71	0.49	2.49	5.82	0.18	16.11	21.80	0.24	0.01	0.21	0.07	99.12
		1σ	1.98	1.42	1.49	0.45	0.26	0.07	0.09	0.26	0.05	0.44	0.58	0.02	0.02	0.06	0.07	
	12	Rim average	83.02	44.80	45.83	9.37	51.73	0.50	2.32	5.86	0.18	16.09	21.88	0.23	0.01	0.22	0.07	99.09
		1σ	1.43	1.23	1.11	0.35	0.21	0.09	0.09	0.20	0.08	0.31	0.51	0.02	0.02	0.07	0.08	
		Core max Mg#	84.05	45.73	45.61	8.66	51.44	0.55	2.42	5.42	0.22	16.02	22.35	0.27	0.01	0.16	0.04	98.90
GT1A_147_1_3-7	13	Core average	83.42	43.82	46.87	9.31	51.57	0.44	2.37	5.81	0.18	16.39	21.32	0.24	0.00	0.31	0.00	98.62
		1σ	2.51	1.74	1.87	0.70	0.61	0.10	0.18	0.42	0.06	0.54	0.70	0.03	0.01	0.09	0.11	
	5	Rim average	83.25	45.11	45.69	9.19	51.73	0.40	2.25	5.75	0.13	16.04	22.03	0.23	0.00	0.37	0.12	99.06
		1σ	2.59	1.29	1.81	0.68	0.34	0.11	0.13	0.41	0.13	0.55	0.46	0.03	0.00	0.16	0.06	
	13	Core max Mg#	84.27	44.71	46.59	8.70	50.62	0.63	2.72	5.39	0.22	16.20	21.63	0.20	0.03	0.43	0.12	98.19
GT1A_152_4_13-17	15	Core average	85.41	44.46	47.43	8.10	52.37	0.41	2.78	5.06	0.14	16.63	21.69	0.29	0.00	0.38	0.03	99.78
		1σ	1.50	1.21	1.10	0.47	0.36	0.05	0.17	0.28	0.03	0.30	0.50	0.03	0.01	0.15	0.02	
	15	Rim average	85.38	43.93	47.87	8.20	52.59	0.47	2.46	5.14	0.16	16.83	21.49	0.26	0.01	0.30	0.01	99.70
		1σ	1.64	1.26	1.24	0.41	0.26	0.03	0.10	0.25	0.03	0.35	0.52	0.02	0.01	0.05	0.01	
	15	Core max Mg#	86.55	45.52	47.15	7.33	52.63	0.31	2.54	4.55	0.17	16.43	22.07	0.31	0.00	0.42	0.00	99.43
GT1A_154_4_61-65	9	Core average	84.07	44.35	46.79	8.86	52.11	0.47	2.31	5.58	0.17	16.52	21.79	0.22	0.00	0.17	0.00	99.35
		1σ	2.44	1.71	1.81	0.61	0.35	0.08	0.25	0.37	0.10	0.53	0.70	0.05	0.01	0.08	0.03	
	6	Rim average	84.17	44.02	47.12	8.86	52.15	0.54	2.39	5.58	0.17	16.63	21.62	0.23	0.00	0.19	0.05	99.53
		1σ	1.68	1.53	1.28	0.54	0.29	0.06	0.07	0.33	0.04	0.35	0.65	0.03	0.02	0.06	0.07	
	9	Core max Mg#	85.51	46.22	45.99	7.79	52.09	0.50	2.50	4.90	0.31	16.22	22.68	0.29	0.00	0.28	0.00	99.77
GT1A_156_1_53-57	9	Core average	83.67	44.50	46.44	9.06	51.46	0.44	2.75	5.66	0.17	16.26	21.68	0.22	0.01	0.50	0.05	99.21
		1σ	3.04	2.22	2.32	0.61	0.74	0.08	0.42	0.35	0.09	0.68	0.91	0.04	0.02	0.13	0.07	
	9	Rim average	83.56	44.82	46.11	9.07	51.82	0.55	2.38	5.67	0.16	16.18	21.88	0.22	0.00	0.32	0.06	99.24
		1σ	1.37	1.30	1.05	0.43	0.28	0.09	0.22	0.26	0.07	0.28	0.55	0.05	0.01	0.04	0.08	
	9	Core max Mg#	84.72	45.58	46.11	8.31	51.54	0.56	2.41	5.23	0.14	16.27	22.38	0.20	0.00	0.39	0.07	99.19
GT2A																		
GT2A_20_3_55-59	9	Core average	81.23	44.95	44.72	10.33	53.34	0.50	2.05	6.56	0.18	15.93	22.28	0.28	0.00	0.07	0.02	101.21
		1σ	2.04	1.75	1.53	0.66	0.48	0.12	0.45	0.40	0.03	0.44	0.74	0.06	0.01	0.04	0.02	
	6	Rim average	79.60	44.95	43.82	11.23	52.14	1.43	2.31	7.03	0.18	15.39	21.96	0.36	0.01	0.06	0.01	100.90
		1σ	4.41	1.94	3.28	0.89	1.59	1.98	0.39	0.50	0.02	1.03	0.61	0.05	0.01	0.03	0.02	
	9	Core max Mg#	82.85	44.84	45.70	9.46	53.21	0.52	2.09	6.03	0.18	16.35	22.32	0.30	0.01	0.09	0.00	101.11
GT2A_35_3_71-75	9	Core average	78.34	44.88	43.18	11.94	52.39	0.66	2.63	7.44	0.21	15.09	21.83	0.37	0.00	0.05	0.01	100.68
		1σ	1.05	0.59	0.78	0.30	0.41	0.07	0.24	0.18	0.02	0.24		0.05	0.00	0.02	0.01	
	6	Rim average	78.12	43.69	43.99	12.32	52.30	0.69	2.52	7.71	0.23	15.44	21.34	0.38	0.00	0.02	0.01	100.64
		1σ	0.92	1.17	0.69	0.53	0.60	0.10	0.22	0.32	0.04	0.15	0.51	0.04	0.00	0.03	0.01	
	9	Core max Mg#	78.86	45.94	42.63	11.43	51.93	0.76	3.02	7.11	0.20	14.87	22.30	0.37	0.00	0.07	0.00	100.61
GT2A_46_3_56-60	9	Core average	79.07	41.69	46.10	12.20	53.46	0.64	2.61	7.72	1.55	16.36	20.59	0.32	0.00	0.04	0.01	103.30
		1σ	4.55	4.14	3.75	1.64	0.51	0.08	0.21	0.96	1.14	1.06	1.78	0.04	0.00	0.03	0.01	
	3	Rim average	78.29	42.31	45.17	12.52	52.95	0.71	2.75	7.91	2.57	16.00	20.85	0.34	0.00	0.01	0.00	104.09
		1σ	2.52	2.44	2.15	0.77	0.67	0.20	0.22	0.43	2.01	0.61	1.05	0.05	0.00	0.02	0.00	
	9	Core max Mg#	80.80	44.52	44.83	10.65	53.37	0.61	2.63	6.74	0.84	15.90	21.97	0.30	0.00	0.05	0.00	102.40
GT2A_46_4_47-51	9	Core average	78.49	43.80	44.12	12.09	52.79	0.63	2.60	7.61	0.19	15.58	21.52	0.35	0.00	0.02	0.01	101.31
		1σ	1.31	1.08	1.01	0.46	0.66	0.11	0.32	0.27	0.02	0.29	0.45	0.01	0.01	0.02	0.02	
	6	Rim average	78.36	44.59	43.42	11.99	52.76	0.73	2.63	7.52	0.21	15.28	21.83	0.38	0.00	0.03	0.01	101.40
		1σ	0.88	0.88	0.68	0.35	0.36	0.03	0.12	0.20	0.03	0.18	0.38	0.02	0.00	0.02	0.02	
	9	Core max Mg#	79.35	44.39	44.13	11.49	53.60	0.49	2.20	7.28	0.21	15.69	21.96	0.34	0.01	0.01	0.00	101.79
GT2A_50_1_47-51	9	Core average	78.87	43.72	44.39	11.89	52.97	0.61	2.39	7.50	0.19	15.70	21.52	0.34	0.00	0.03	0.02	101.27
		1σ	1.30	1.38	0.96	0.65	0.68	0.15	0.45	0.40	0.02	0.24	0.60	0.04	0.00	0.03	0.02	
	6	Rim average	78.52	44.51	43.57	11.92	52.46	0.73	2.54	7.48	0.22	15.35	21.81	0.38	0.01	0.04	0.01	101.03
		1σ	1.87	1.71	1.38	0.80	0.56	0.06	0.16	0.48	0.03	0.38	0.72	0.03	0.00	0.02	0.02	
	9	Core max Mg#	80.08	44.43	44.50	11.07	53.75	0.39	1.69	7.06	0.19	15.92	22.11	0.31	0.00	0.00	0.08	101.49
GT2A_52_3_25-29	9	Core average	78.79	44.90	43.42	11.69	51.41	0.65	2.43	7.34	0.21	15.29	22.00	0.34	0.00	0.04	0.00	99.70
		1σ	2.06	1.36	1.51	0.67	0.53	0.18	0.51	0.40	0.03	0.46	0.54	0.07	0.00	0.03	0.01	
	6	Rim average	76.95	39.72	46.38	13.89	48.83	0.88	5.37	8.28	0.19	15.50	18.47	0.97	0.06	0.04	0.00	98.59
		1σ	3.76	11.88	5.33	3.26	3.64	0.27	4.33	1.70	0.04	0.25	5.11	0.93	0.09	0.03	0.01	
	9	Core max Mg#	80.94	44.79	44.69	10.52	51.96	0.41	1.61	6.69	0.20	15.95	22.24	0.25	0.00	0.05	0.00	99.35

Table 3c. (Continued)

Hole_Core_Section_Interval	n		Mg#	Wo	En	Fs	SiO$_2$	TiO$_2$	Al$_2$O$_3$	FeO	MnO	MgO	CaO	Na$_2$O	K$_2$O	Cr$_2$O$_3$	NiO	Total
GT2A_75_3_8-12	9	Core average	79.44	42.69	45.53	11.78	52.90	0.72	2.75	7.42	0.20	16.08	20.98	0.38	0.00	0.05	0.00	101.48
		1σ	2.85	2.84	2.29	1.13	0.50	0.05	0.14	0.67	0.02	0.62	1.22	0.04	0.00	0.04	0.01	
	6	Rim average	80.08	43.90	44.92	11.17	52.70	0.66	2.54	7.04	0.17	15.89	21.60	0.40	0.00	0.04	0.01	101.05
		1σ	1.84	1.84	1.43	0.72	0.30	0.05	0.14	0.43	0.04	0.39	0.79	0.04	0.00	0.03	0.02	
	9	Core max Mg#	80.82	44.93	44.51	10.56	52.94	0.71	2.60	6.69	0.23	15.82	22.22	0.39	0.00	0.05	0.00	101.65
GT2A_86_2_33-37	9	Core average	81.89	45.02	45.02	9.96	52.15	0.48	2.35	6.27	0.16	15.92	22.15	0.31	0.00	0.04	0.01	99.85
		1σ	1.36	1.46	0.88	0.76	0.60	0.13	0.48	0.47	0.03	0.19	0.63	0.05	0.00	0.03	0.02	
	6	Rim average	81.69	45.09	44.86	10.05	51.83	0.55	2.12	6.33	0.18	15.84	22.15	0.34	0.00	0.04	0.02	99.40
		1σ	1.56	1.09	0.97	0.75	0.82	0.19	0.53	0.47	0.04	0.26	0.44	0.04	0.00	0.04	0.02	
	9	Core max Mg#	84.77	47.12	44.83	8.05	53.06	0.24	1.18	5.14	0.21	16.04	23.46	0.22	0.00	0.04	0.05	99.64
GT2A_102_1_3-7	9	Core average	85.35	43.86	47.91	8.22	51.52	0.39	2.63	5.18	0.12	16.95	21.59	0.26	0.00	0.30	0.02	98.97
		1σ	4.17	3.46	3.27	0.84	0.28	0.04	0.22	0.48	0.02	0.93	1.46	0.03	0.00	0.05	0.03	
	6	Rim average	83.87	45.05	46.09	8.86	50.77	0.49	2.37	5.50	0.18	16.04	21.82	0.31	0.00	0.24	0.01	97.74
		1σ	3.86	1.45	2.79	0.45	0.99	0.09	0.30	0.24	0.01	0.87	0.40	0.02	0.00	0.02	0.02	
	9	Core max Mg#	86.30	45.43	47.10	7.47	51.60	0.35	2.19	4.72	0.11	16.70	22.41	0.24	0.00	0.28	0.00	98.61
GT2A_104_1_5-9	9	Core average	84.47	44.48	46.89	8.62	51.49	0.40	2.36	5.46	0.16	16.66	21.99	0.28	0.00	0.19	0.01	99.01
		1σ	1.97	2.04	1.54	0.63	0.40	0.04	0.29	0.38	0.03	0.41	0.89	0.04	0.00	0.03	0.01	
	6	Rim average	83.87	44.85	46.26	8.89	51.11	0.60	2.42	5.60	0.17	16.33	22.03	0.31	0.00	0.19	0.02	98.78
		1σ	1.39	1.02	0.98	0.48	0.17	0.03	0.14	0.29	0.05	0.28	0.42	0.02	0.00	0.05	0.01	
	9	Core max Mg#	85.57	45.96	46.24	7.80	52.12	0.33	1.60	5.01	0.15	16.67	23.06	0.18	0.00	0.18	0.00	99.30
GT2A_104_4_53-57	9	Core average	84.93	45.17	46.57	8.26	52.79	0.43	2.18	5.28	3.27	16.68	22.51	0.28	0.00	0.22	0.01	103.65
		1σ	1.11	1.14	0.79	0.47	0.55	0.09	0.41	0.29	1.43	0.20	0.50	0.07	0.00	0.09	0.02	
	3	Rim average	84.40	45.72	45.81	8.47	52.50	0.43	1.87	5.39	2.25	16.37	22.73	0.31	0.00	0.22	0.03	102.10
		1σ	0.63	0.89	0.54	0.22	0.59	0.05	0.19	0.13	0.55	0.13	0.39	0.01	0.00	0.01	0.03	
	9	Core max Mg#	85.89	45.00	47.24	7.76	52.46	0.42	2.60	4.88	2.47	16.67	22.09	0.35	0.00	0.36	0.00	102.29
GT2A_105_2_39-43	9	Core average	78.38	42.04	45.43	12.53	51.69	0.72	2.43	7.88	0.23	16.02	20.63	0.37	0.00	0.12	0.02	100.10
		1σ	3.67	3.76	3.01	1.52	0.45	0.04	0.16	0.90	0.03	0.81	1.62	0.04	0.00	0.05	0.02	
	6	Rim average	78.73	44.35	43.82	11.83	51.40	0.73	2.54	7.43	0.22	15.42	21.72	0.41	0.00	0.14	0.02	100.03
		1σ	0.74	0.52	0.50	0.34	0.48	0.04	0.06	0.21	0.02	0.14	0.21	0.03	0.01	0.03	0.02	
	9	Core max Mg#	79.75	45.26	43.66	11.08	51.89	0.67	2.13	7.01	0.28	15.48	22.33	0.37	0.00	0.11	0.05	100.31
GT2A_117_2_6-10	9	Core average	79.65	44.21	44.44	11.35	52.66	0.65	2.55	7.10	0.19	15.59	21.59	0.36	0.00	0.18	0.01	100.87
		1σ	1.93	1.25	1.26	0.92	0.59	0.12	0.43	0.56	0.03	0.35	0.49	0.03	0.01	0.05	0.02	
	6	Rim average	80.13	44.09	44.80	11.11	52.79	0.65	2.50	6.95	0.19	15.72	21.53	0.37	0.00	0.19	0.02	100.92
		1σ	2.28	1.60	1.49	1.11	0.72	0.15	0.54	0.68	0.03	0.41	0.64	0.05	0.00	0.07	0.02	
	9	Core max Mg#	81.96	44.97	45.10	9.93	53.00	0.51	1.90	6.27	0.17	15.97	22.16	0.32	0.00	0.13	0.00	100.41

4 Analytical results

Textural variations of Hole GT1A and GT2A gabbros

Descriptions of microtextures of gabbros

The shape-preferred orientation of crystals and aligned aggregates of constituent minerals made up the foliation and lineation of both GT2A and GT1A gabbros. The asymmetric microstructures of crystals are ubiquitous and caused by grain boundary sliding originated from dislocation creep. The most abundant rock types in holes GT1A and GT2A are olivine gabbros and olivine-bearing gabbros. These gabbroic rocks are essentially composed of olivine, plagioclase and clinopyroxene. Olivine occurs mostly as anhedral equant to elongated crystals with kink bands, partially altered to serpentine, talc and magnetite. Elongated aggregates of olivine are common in the lowermost GT2A and lower half of GT1A. Plagioclase is classified into three types: primary, broken and recrystallized. Primary plagioclase preserves igneous subhedral to euhedral platy to stubby forms characterized by almost straight outlines, relatively homogeneous cores surrounded by normally zoned rims, and ubiquitous inclusions (Figure 2a). Ophitic plagioclase laths included in clinopyroxene also preserve primary igneous morphology (Figure 2b). Most cumulus plagioclase crystals are broken into two or more pieces, which are identified by truncated zoning and embayed outlines (Figure 2c). Anhedral equant grains in contact with each other at 120° triple junctions are recrystallized plagioclases, which are unzoned and have rare inclusions (Figure 2d). Clinopyroxene is commonly anhedral to subhedral, and it contains enclosing a few small inclusions of plagioclase. Ophitic clinopyroxenes enclosing thin plagioclase laths are not many, but they are present throughout both holes, regardless of the stratigraphic height. Clinopyroxene crystals are divided into primary crystals, subgrains, neoblasts and recrystallized grains. Primary crystals preserve the intact, igneous forms with or without subgrains (Figure 2e), and some are deformed with a quarter structure (Figure 2f). Sub-grains are present surrounding larger crystals with different extinction angles of less than 15 degrees against the adjacent crystals. Neoblasts are small discrete single grains, transformed from sub-grains by high-angle rotation and following dislocation (Figure 2g). Recrystallized crystals are texturally equilibrated with very few inclusions (Figure 2h).

Primary and broken cumulus plagioclases have a high-Ca core with a resorbed and embayed outline, which is enveloped by a euhedral to subhedral low-Ca rim (Figure 3a, 3b). Cumulus clinopyroxene also shows zoning consisting of a low-Ti core with resorbed outline, surrounded by a high-Ti rim with subhedral to anhedral outlines (Figure 3c, 3d, 3e, 3f). The transitions of Ca in plagioclase and Ti in clinopyroxene from the core to the rim are relatively sharp and occur within a few tens of micrometers. However, the Mg concentration in clinopyroxene is very uniform and not zoned like Ti (Figure 3). This is ascribed to the faster diffusion rate of Mg in clinopyroxene than Ti (Brandy and McCallister, 1983; Cherniak and Liang, 2012), that erased the Mg zoning but left the Ti zoning through the post-crystallization diffusion.

18   The magmatic conditions and hypersolidus deformation of lower crustal magma chamber
below a fast-spreading ridge — Insight from the core analyses of the Oman ICDP drill holes
GT1A & GT2A
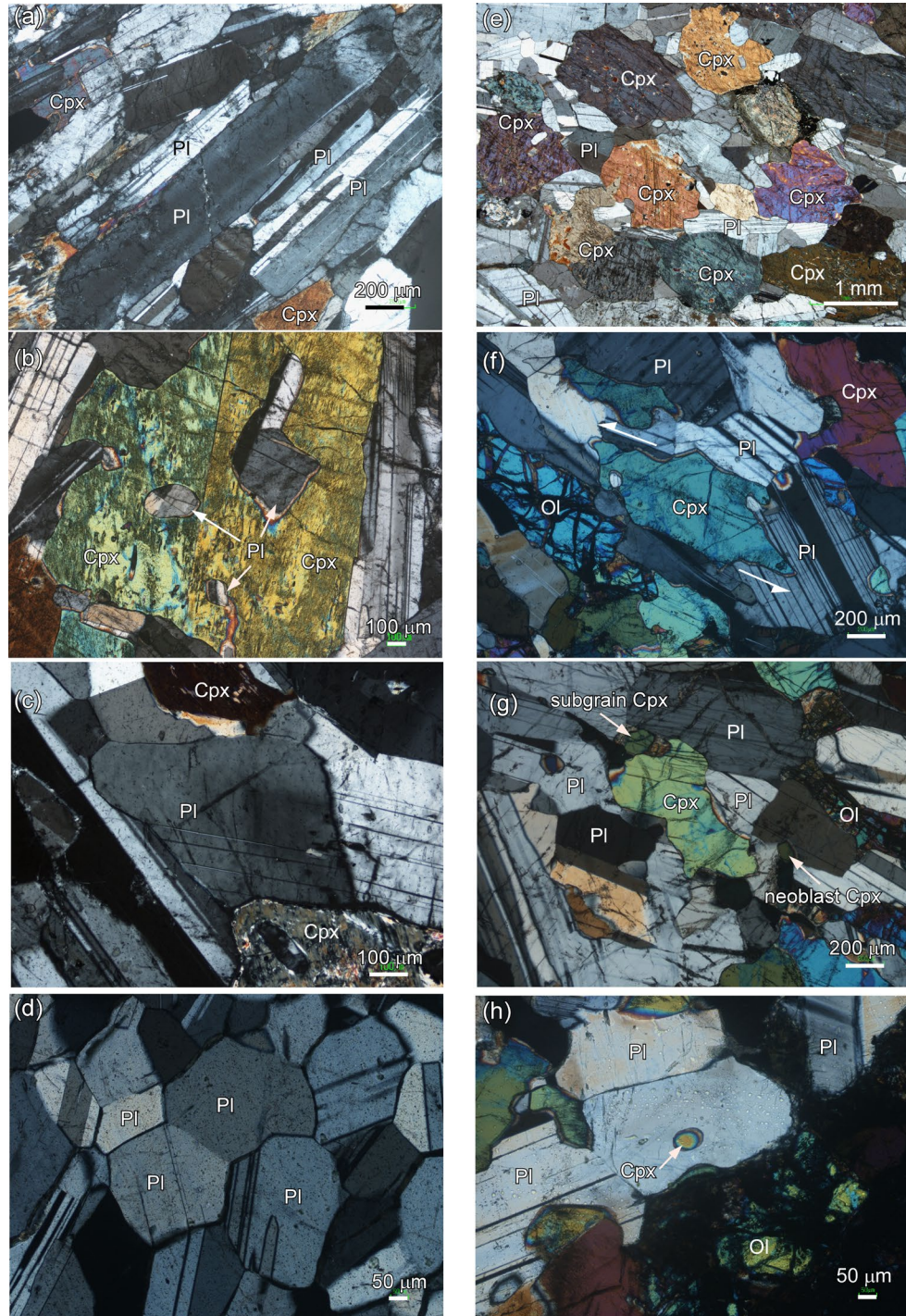
Figure 2. Microphotos of gabbroic core samples from Hole GT1A and GT2A showing varieties of plagioclase (a, primary; b, ophitic; c, broken; d, recrystallized) and clinopyroxene (e, primary; f, quarter structure; g, subgrain and neoblast; h, recrystallized). Arrows in f indicate the shear direction. Hole-Core-Section and Intervals (depth in mbs) of the samples are GT2A-20Z-3, 55-59 cm (44.49 mbs) (a, b), GT2A-46Z-4, 47-51 cm (121.19 mbs) (c), GT2A-50Z-1, 47-51 cm (130.77 mbs) (d), GT2A-35Z-3, 71-75 cm (90.10 mbs) (e), GT1A-45Z-2, 43-47 cm (104.74 mbs) (f), GT1A-152Z-4, 13-17 cm (392.49 mbs) (g), GT2A-117Z-2, 6-10 cm (314.36 mbs) (h). Pl, Cpx, Ol is the abbreviation plagioclase, clinopyroxene, olivine.
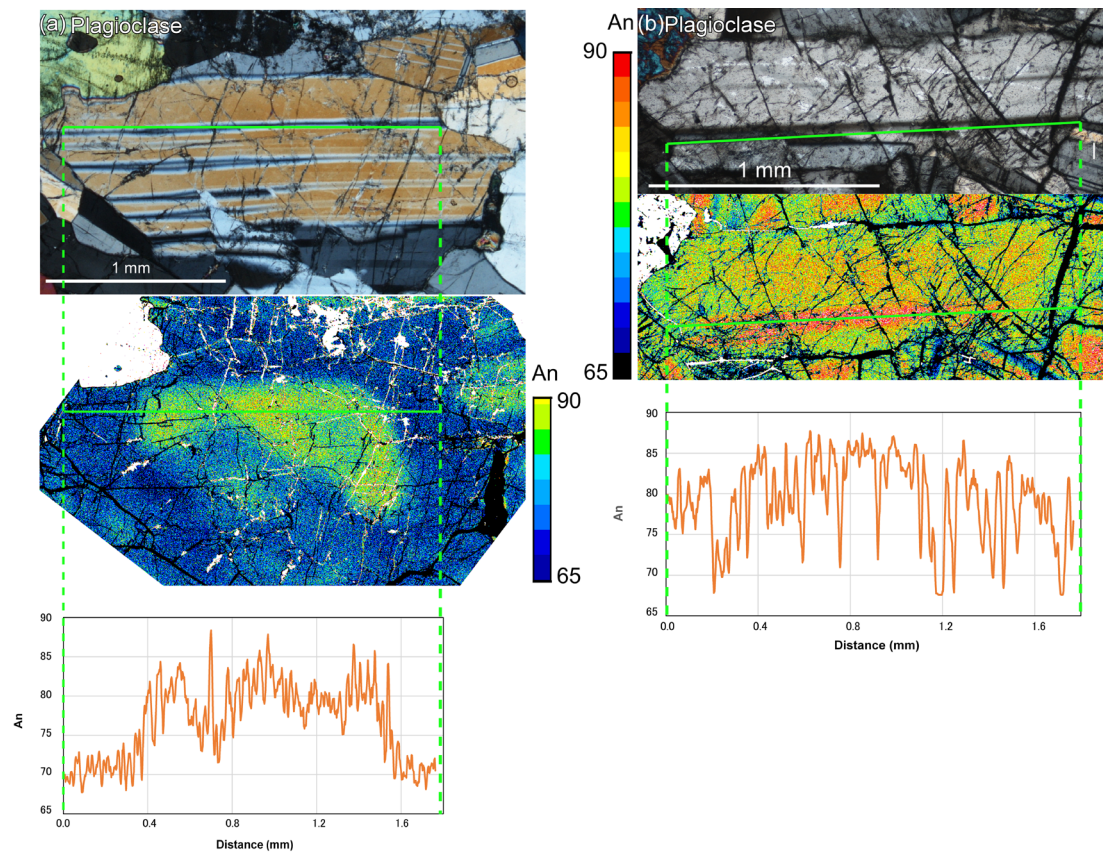
Figure 3. X-ray intensity maps showing zonings of cumulus plagioclase and clinopyroxene. GT1A-30Z-4, 59-63 cm (72.77 mbs) (a), GT2A-20Z-3, 55-59 cm (44.49 mbs) (b), GT1A-30Z-4, 59-63 cm (72.77 mbs) (c), GT2A-104Z-1, 5-9 cm (280.02 mbs) (d), GT2A-46Z-3, 56-60 cm (120.32mbs) (e, f).

20   The magmatic conditions and hypersolidus deformation of lower crustal magma chamber
          below a fast-spreading ridge — Insight from the core analyses of the Oman ICDP drill holes
                                      GT1A & GT2A
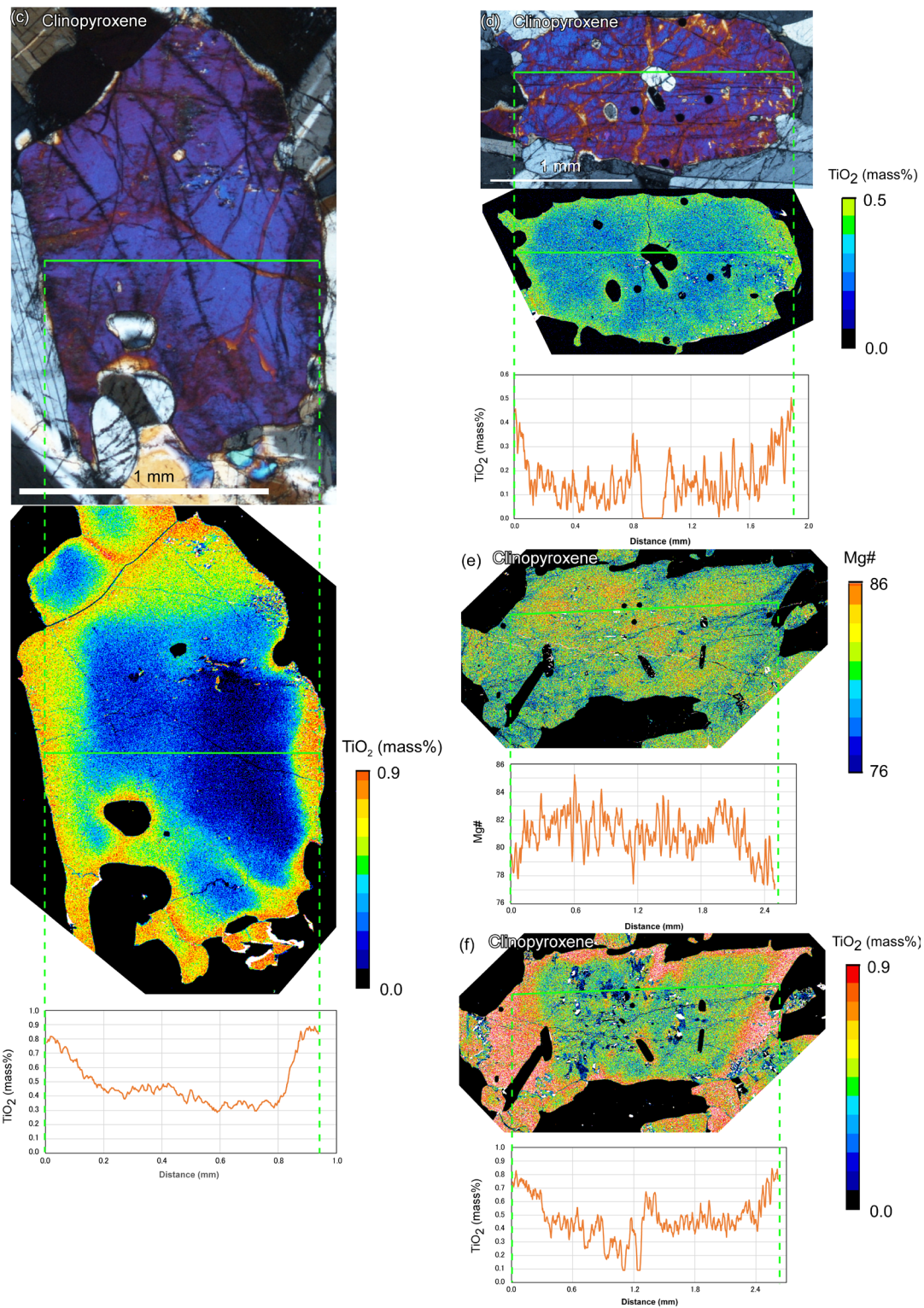
Figure 3. (Continued)

Downhole variations of cumulus plagioclase and clinopyroxene

The average aspect ratio of primary plagioclase decreases from more than 5.0 to 2.0 in the upper 250 m of GT2A, and remains about 2.0 further downhole (Figure 4a, 4b). However, the average aspect ratio is almost constant and less than 2.0 in GT1A except for the uppermost 100 m with slightly higher ratios up to 2.5 (Figure 4a, 4b).

Among the three types of plagioclase, the proportion of primary, cumulus plagioclase decreases from more than 70% to around 3% in GT2A, and from about 7% to less than 1% in GT1A, while that of broken plagioclase increases from approximately 25% to 95%, and from nearly 85% to 90% in GT2A and GT1A, respectively (Figure 4c, 4d). The proportion of recrystallized plagioclase crystals ranges from 0% to 5% in GT2A, smaller than that in GT1A ranging from 5% to 10% (Figure 4e, 4f). Clinopyroxene is deformed to distorted rectangular shapes with a quarter structure, and then changes into crystals with sub-grains, which eventually forms neoblasts. Equilibrium texture shown by polygonal crystals that meet at a triple junction of obtuse angles around 120º appears in downhole. The percentage of primary clinopyroxene in GT2A decreases from 100% to 90% in the uppermost 100 m, remaining almost around 90% down to 240 mbs, and then decreases to 80% at 320 mbs (Figure 4g). In GT1A, it steadily decreases from 90% to 60% in the interval from 70 mbs to 400 mbs (Figure 4h). In contrast, secondary clinopyroxene crystals, including subgrains, neoblasts, and recrystallized grains, tend to be higher downhole in both holes. The proportion of subgrain varies between 4% to 10% in GT2A, and from 9% to 13% in GT1A. Neoblasts are absent in the upper 200 m and 100 m and increase to 12% to 13% downhole in GT2A and GT1A, respectively. Texturally equilibrated, recrystallized grains appear only in the lower 100 m and 200 m in GT2A and GT1A, respectively (Figure 4i, 4j) (Table 1).

Whole rock geochemistry and its downhole variations

Downhole variations of whole-rock compositions are consistent with the range of the onboard data with the GT1A cores less evolved than the GT2A cores (Figure 5). Mg#s show no systematic changes downhole and vary between 70 and 80 in Hole GT2A (Figure 5a) and between 75 and 85 in Hole GT1A (Figure 5b). Cr contents are generally lower than 500 μg/g in Hole GT2A (Figure 5g), and lower than 1000 μg/g in Hole GT1A (Figure 5h), except for some high Cr intervals. La in GT1A cores is steady and generally lower than GT2A cores, varying between 0.1 μg/g and 0.3 μg/g (Figure 5f). La in GT2A cores shows more varied from 0.2 μg/g to 0.4 μg/g, with a downhole decrease in the upper 150 m (Figure 5e).

Chondrite-normalized rare earth element (REE) concentrations decrease sharply from Eu to La and increase slightly from Lu to Gd (Figures 6a, 6b). Hole GT1A and GT2A core samples largely overlap in REEs, but the positive Eu anomalies is stronger in GT2A and the Ta depression is larger in some GT1A samples. Light REEs (LREEs) and Zr are depleted relative to the primitive mantle in both holes (Figures 6c). Melt compositions in equilibrium with the clinopyroxene of GT1A samples largely overlap with the V1 sheeted dike compositions but some melts in equilibrium with clinopyroxene cores are more primitive than the sheeted dikes. Equilibrium melts with the GT2A clinopyroxenes overlap with the differentiated sheeted dikes. Melts in equilibrium with clinopyroxene rims are generally more differentiated than those of cores from both holes.

22   The magmatic conditions and hypersolidus deformation of lower crustal magma chamber
below a fast-spreading ridge — Insight from the core analyses of the Oman ICDP drill holes
GT1A & GT2A
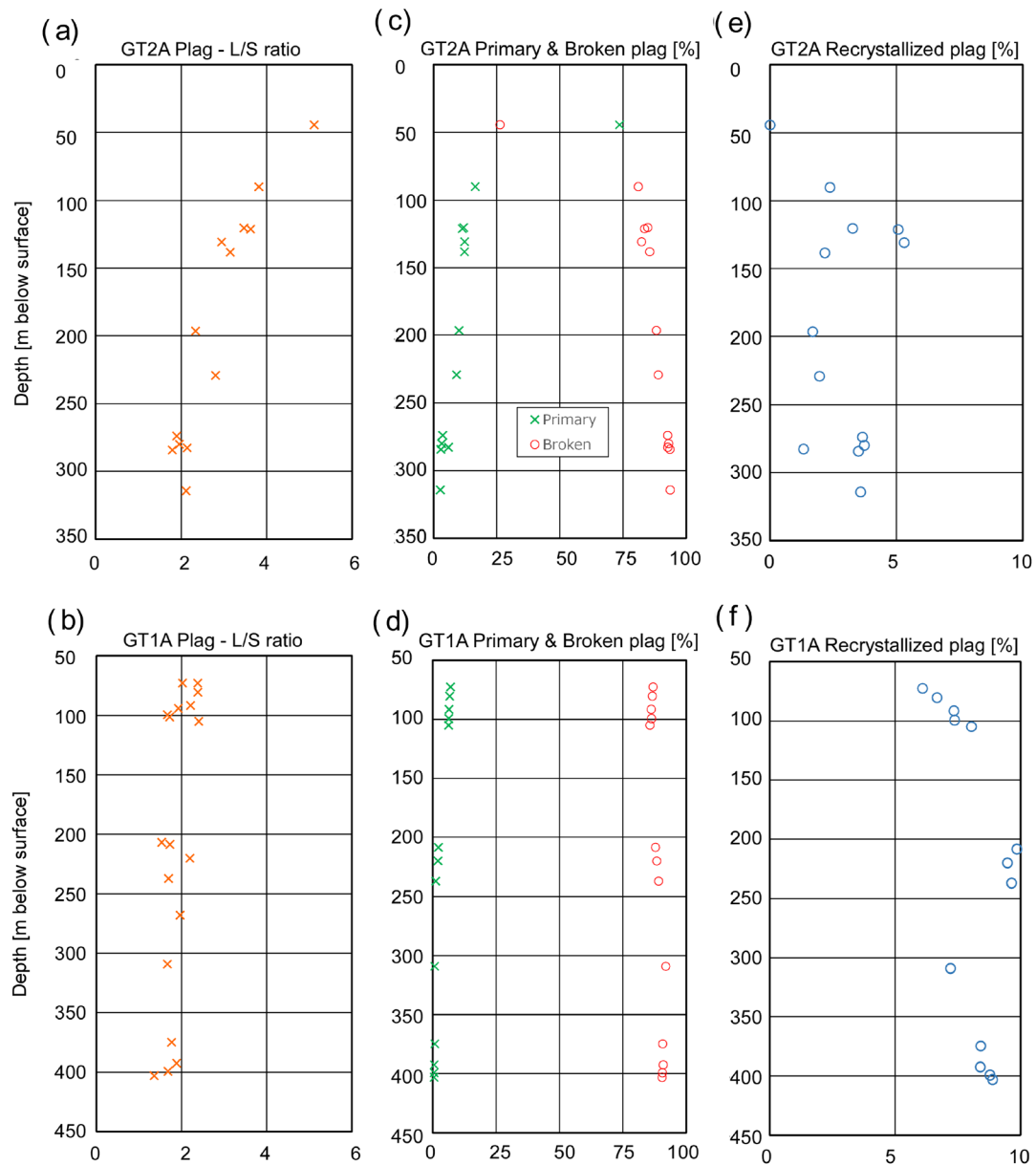
Figure 4. Downhole variations of plagioclase aspect ratios (a, b) and types (c-f) and clinopyroxene types (g-j).
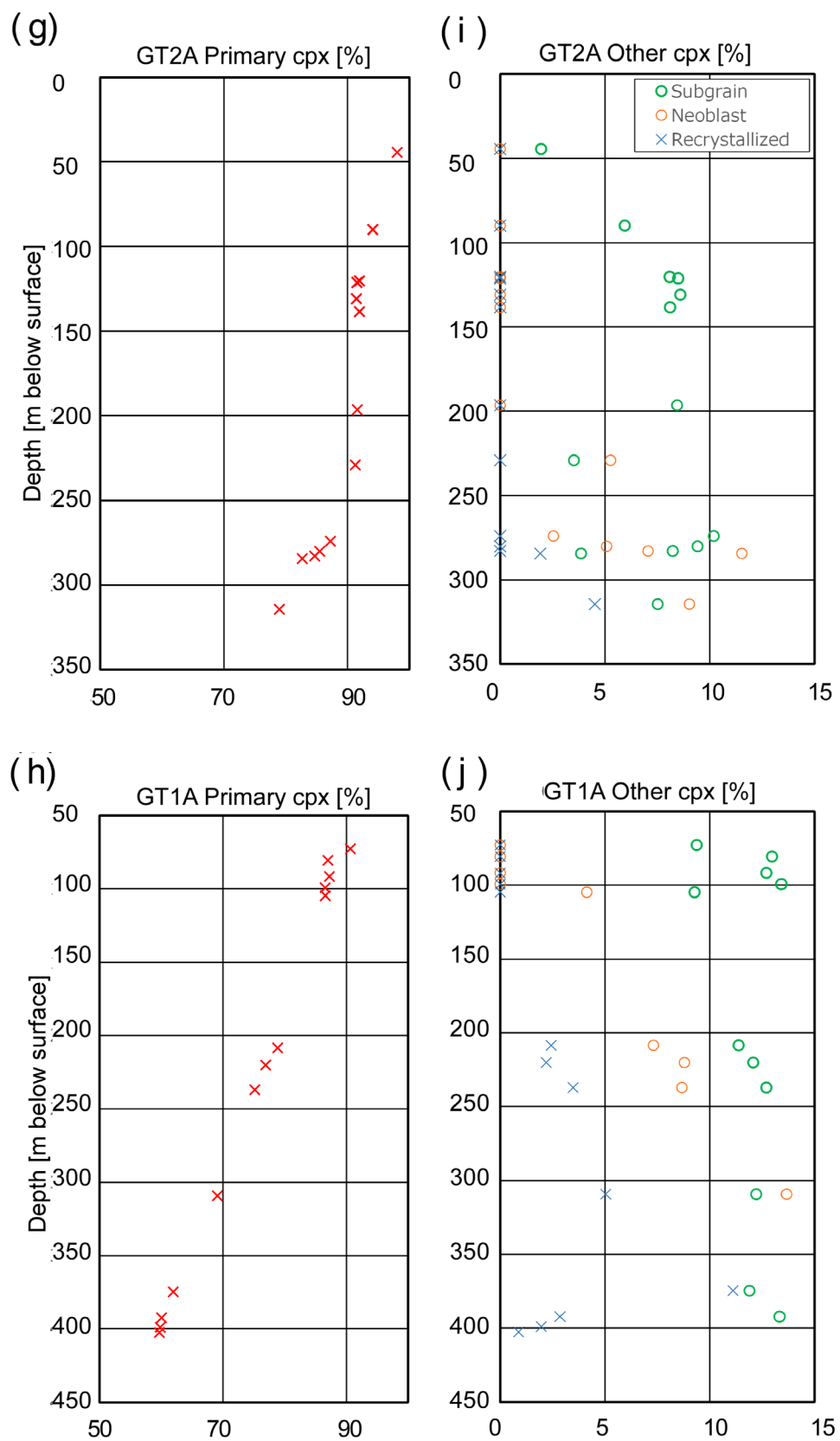
Figure 4. (Continued)
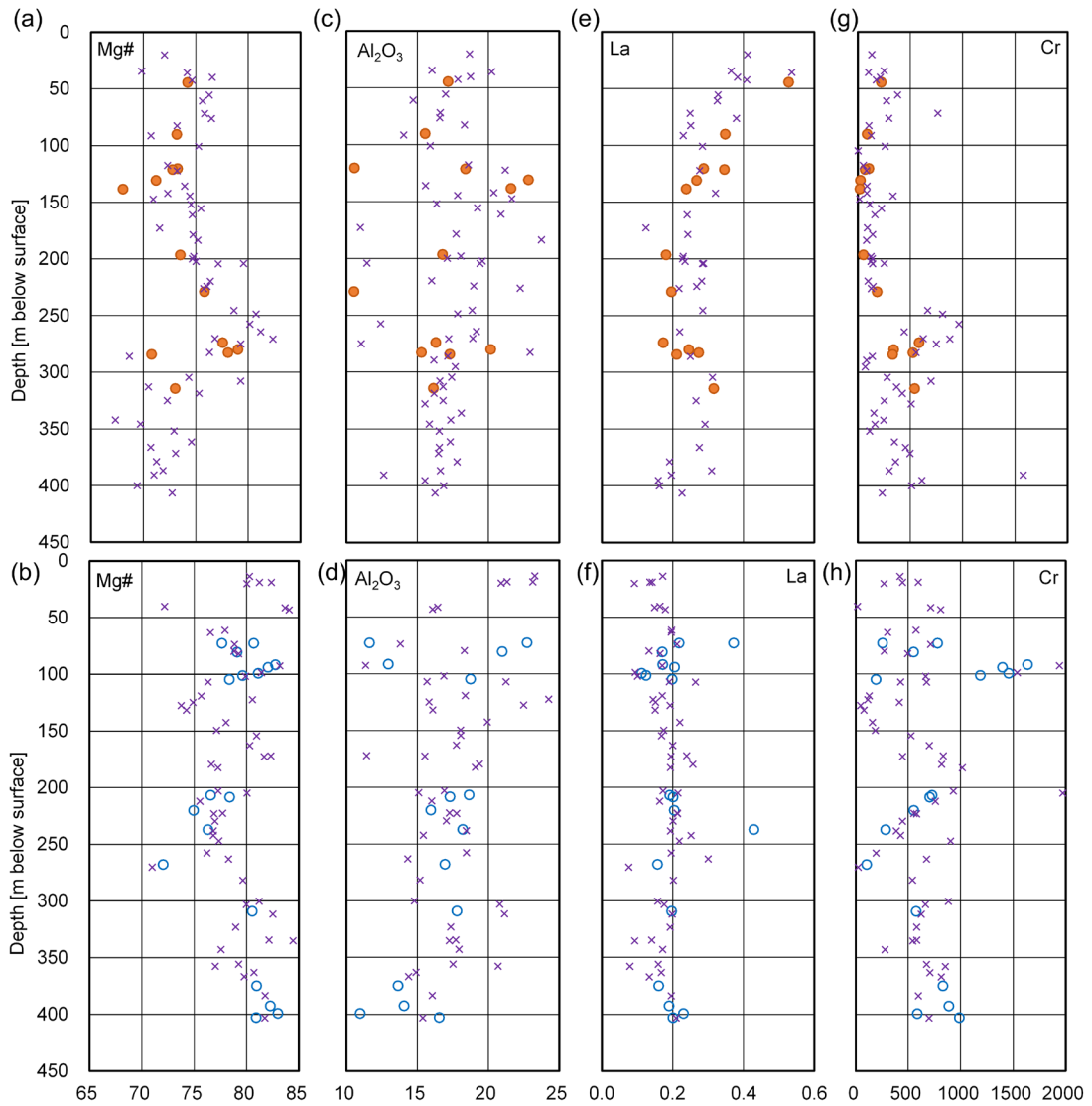
Figure 5. Stratigraphic variations of the whole-rock Mg# (a, b), Al_2O_3 (mass%) (c, d), La and Cr (μg/g) (e-h) in Hole GT2A and GT1A. Circles, this study; crosses, Kelemen et al. (2020a, b).
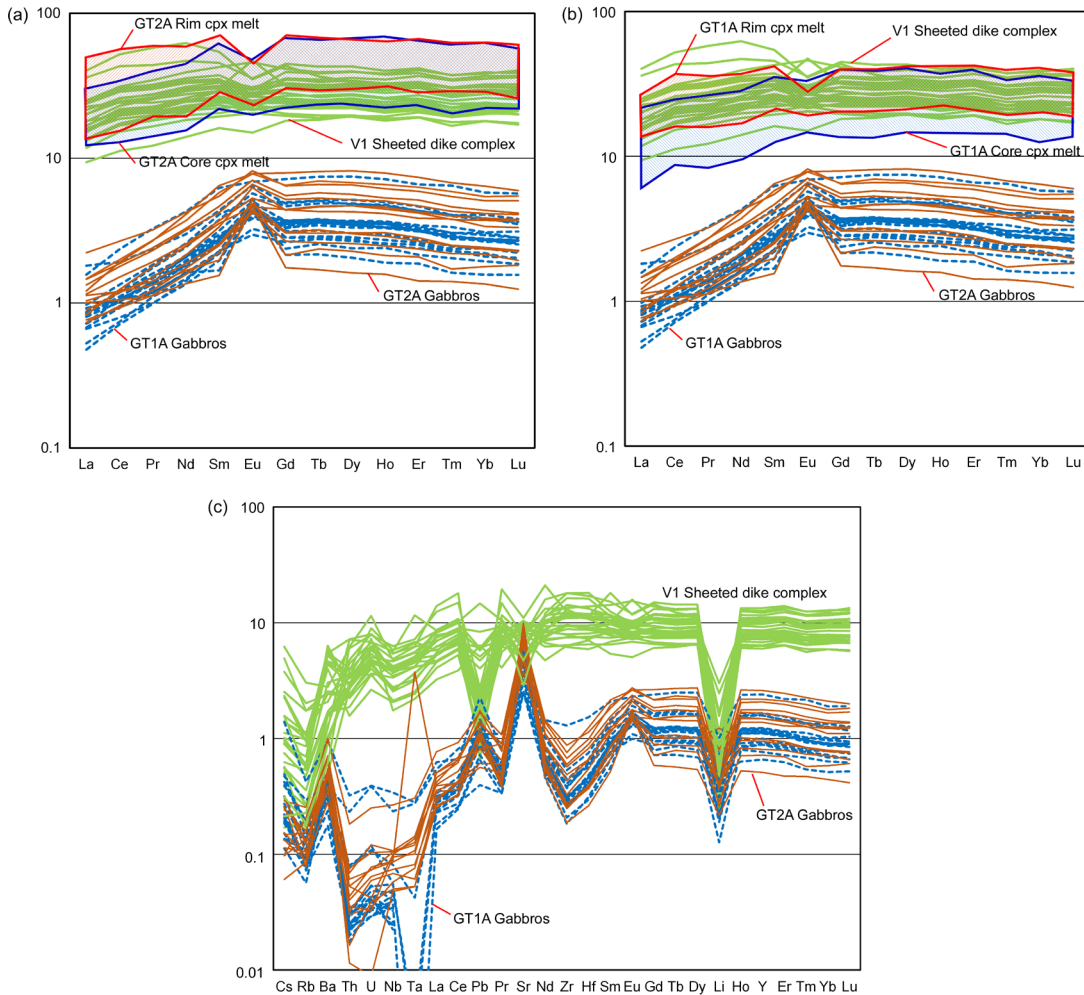
Figure 6. Chondrite normalized rare earth elements (a, b) and primitive mantle normalized trace elements (c) of the gabbroic core samples from Hole GT1A (solid lines) and GT2A (broken lines), and the V1 sheeted dike complex (bold lines), and primitive melt in equilibrium with clinopyroxene cores and rims in the two holes (shaded areas). Normalizing factors after Sun and McDonough (1989), partition coefficients after Workman and Hart (2005).

Mineral chemistry and its downhole variations

Cumulus clinopyroxene and olivine have higher Mg#s in GT1A than in GT2A, which is consistent with the whole-rock data (Figure 7). Olivine cores decrease in Ni from 0.12 mass% to 0.03 mass% with the decrease in Mg# from 82.5 to 72.7 (Figure 7g). With the decreasing Mg# from 90 to 75, clinopyroxene cores increase in TiO_2 from 0.38 mass% to 0.77 mass% in GT1A and from 0.39 mass% to 0.88 mass% in GT2A (Figure 7d), and decrease in Cr_2O_3 from 0.69 mass% to 0.07 mass% in GT1A and from 0.30 mass% to 0.01 mass% in GT2A (Figure 7f). GT1A clinopyroxene cores decrease in Al_2O_3 from 3.3 to 2.3, whereas GT2A clinopyroxene cores first decrease and then increase in Al_2O_3 with the decreasing Mg# (Figure 7e). Zoning in clinopyroxene is discerned by comparing Mg#s between core and rim of each cumulus crystal. Both normal and reverse

26   The magmatic conditions and hypersolidus deformation of lower crustal magma chamber
                below a fast-spreading ridge — Insight from the core analyses of the Oman ICDP drill holes
                                              GT1A & GT2A

zonings are present in GT1A and GT2A, where fifteen over 31 crystals are normally zoned, and 8 crystals are reversely zoned (Figure 7a). With decreasing An, Fe content of plagioclase of both holes increases until An_{77}, and then decreases in GT2A (Figure 7c). Mg# and An mol% of coexisting clinopyroxene and plagioclase pairs plot subparallel to but are higher in An than those of Pito Deep gabbro. However, the plagioclase-clinopyroxene pairs of Hess Deep gabbro largely scatter and overlap the Oman pairs with low Mg#s and An contents (Figure 7b).
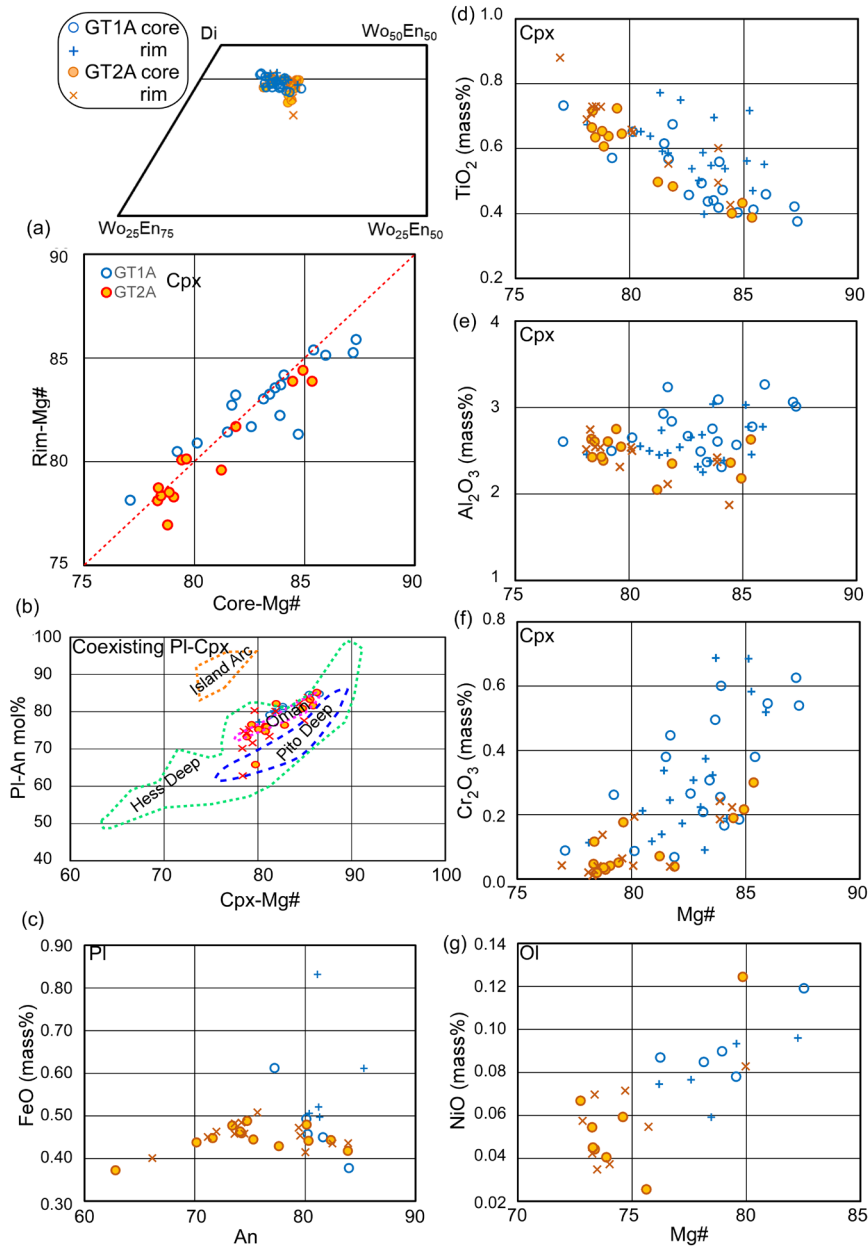
Figure 7. Clinopyroxene (Cpx), olivine (Ol) and plagioclase (Pl) core and rim compositions from Hole GT1A and GT2A. Data for the Pito Deep (Perk et al., 2007), the Hess Deep (Dick and Natland, 1996; Miller et al., 1996; Natland and Dick, 1996; Gillis et al., 2014; Lissenberg et al., 2013), the island arcs (St. Vincent, Tollan et al., 2011; Raoul Island, Haase et al., 2014) and the Oman ophiolite by Koepke el al. (2022).
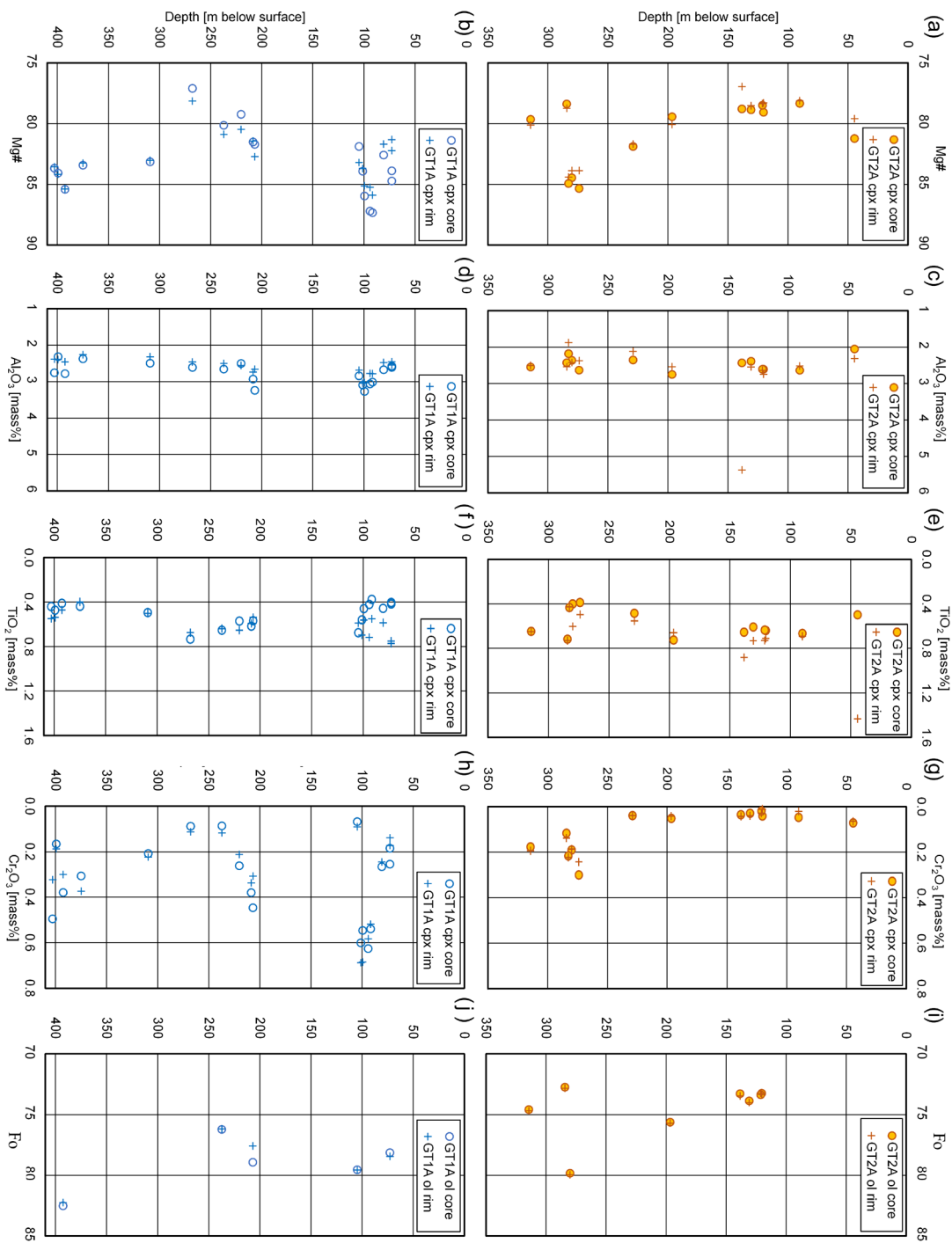
Figure 8. Stratigraphic variations of clinopyroxene Mg#, Al_2O_3, TiO_2 and Cr_2O_3 (mass%) (a-h), olivine Fo (i, j) in Hole GT2A and GT1A. Circles and crosses are average core and rim compositions.

28   The magmatic conditions and hypersolidus deformation of lower crustal magma chamber
below a fast-spreading ridge — Insight from the core analyses of the Oman ICDP drill holes
GT1A & GT2A

The downhole variations of mineral compositions are consistent with those of the whole rocks (Figure 8). In Hole GT2A, clinopyroxene Mg#s and olivine Fo contents range mostly in 80 ± 2 and 74 ± 2, respectively, with a high-Mg# interval at 274-283 m below surface. Clinopyroxene and olivine in Hole GT1A show higher and wider ranges of Mg# 77-87 and Fo 76-82, respectively, than those in GT2A, but do not steadily increase or decrease downhole as well. Cr_2O_3 and Al_2O_3 contents show similar downhole variations with wider ranges in GT1A than in GT2A.

Estimation of Trapped Melt Fractions

As is shown by the Ti concentration map (Figure 3), clinopyroxene has a relatively homogeneous low-Ti core surrounded by a high-Ti rim. This indicates that the homogeneous low-Ti core crystallized as a cumulus crystal under a small degree of supercooling in the main magma reservoir and crystallized the high-Ti rim from a more differentiated melt. It is likely that the accumulated crystals were compacted, trapping the surrounding melt in the interstitial space. Subsequent crystallization of the trapped melt promoted the evolution of the remaining melt and the formation of a high-Ti rim. The cores would have been in equilibrium with the interstitial melt at the time of entrapment. However, as the contrasting Ti and Mg X-ray intensity maps of clinopyroxene show, the core composition can be modified by the post-crystallization diffusion (Figure 4). Therefore, we use REE concentrations of the clinopyroxene cores for the estimation of trapped melt fractions (TMFs) because diffusion rates of REEs in clinopyroxene below 1150 °C are more than an order of magnitude slower than Ti that still shows the contrasting compositions of the core and rim (Van Orman et al., 2001).

Given the concentrations of an element in crystals, C_A, C_B, C_C, ... C_n, and melt, C_M, and the fractions of crystals and melt, to be x_A, x_B, ... x_N, and x_M, the concentration of the element in the bulk rock, C_{bulk}, is given by the mass balance equation,

$$C_{bulk} = x_A C_A + x_B C_B + \cdots + x_n C_n \quad (1)$$

As core samples are composed of cumulus olivine, clinopyroxene and plagioclase, the above equation is rewritten as,

$$C_{bulk} = x_{ol} C_{ol} + x_{cpx} C_{cpx} + x_{pl} C_{pl} + x_M C_M \quad (2)$$

When the element of interest is light REEs, olivine can be eliminated from the equation because olivine is virtually free of LREEs. By using partition coefficients of the element of interest between clinopyroxene and melt, and between plagioclase and melt, equation (2) can be rewritten as,

$$C_{bulk} = x_{cpx} D_{cpx} C_M + x_{pl} D_{pl} C_M + x_M C_M \quad (3)$$

The liquid composition C_M can be estimated by using the clinopyroxene composition determined by LA-ICP-MS and clinopyroxene-melt partition coefficient. By applying equations (3) for lathanum, cerium and praseodymium concentrations, we get the following equations (4) to (6) on the trapped melt fraction (TMF), x_M,

$$C_{bulk}^{La} = \left(x_{cpx} D_{cpx}^{La} + x_{pl} D_{pl}^{La} + x_M \right) C_M^{La} \quad (4)$$
$$C_{bulk}^{Ce} = \left(x_{cpx} D_{cpx}^{Ce} + x_{pl} D_{pl}^{Ce} + x_M \right) C_M^{Ce} \quad (5)$$
$$C_{bulk}^{Pr} = \left(x_{cpx} D_{cpx}^{Pr} + x_{pl} D_{pl}^{Pr} + x_M \right) C_M^{Pr} \quad (6)$$

By solving the equations (4), (5), (6) simultaneously, we have estimated the TMF, x_M. The estimated TMFs in Table 4 are based on the minimum and the average REE concentrations in clinopyroxene cores, which give the maximum and the average TMFs (Figure 9). Except for the highest TMF of 19.5 mass% in hole GT1A, the TMF falls between 1 mass% and 7 mass% in both GT1A and GT2A holes, with most data points plotted between 1 mass% and 5 mass%. The TMF shows no systematic variation within or between both drill holes.
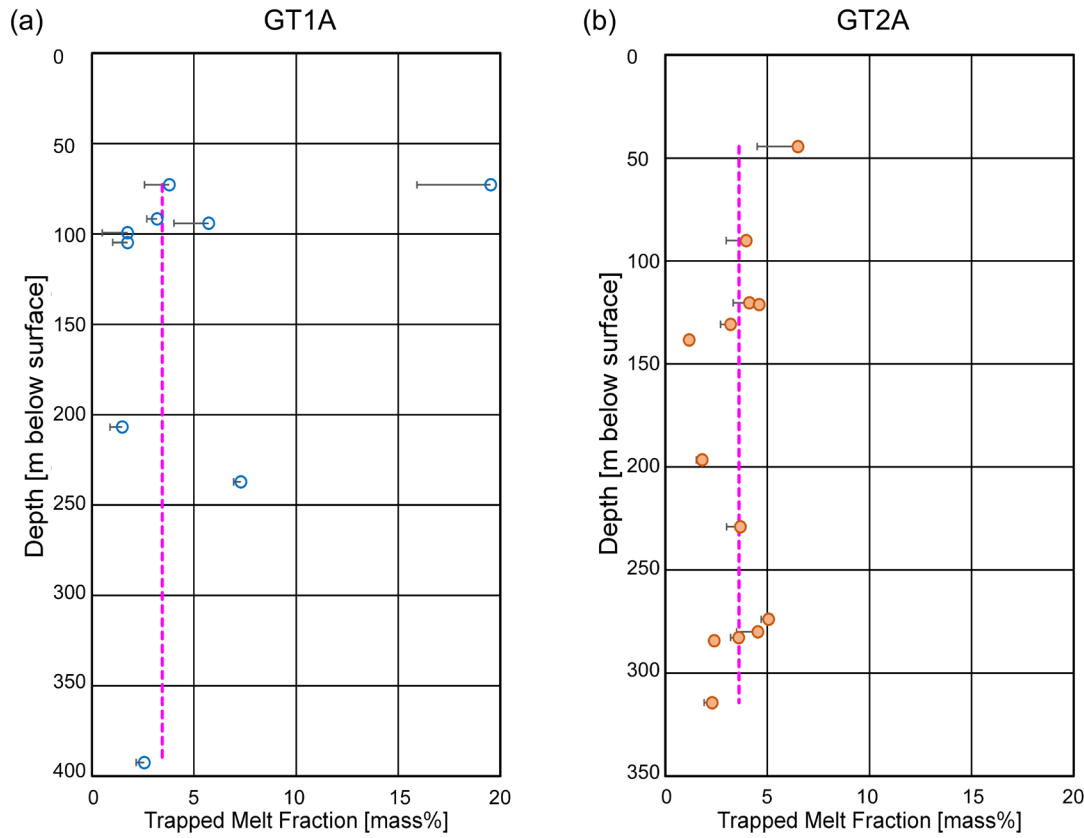
Figure 9. Downhole variations of trapped melt fractions (TMFs) in Hole GT1A (a) and GT2A (b) estimated based on the La, Ce and Pr concentrations of clinopyroxene cores in gabbros. Short horizontal bars connect the TMF estimates for the average and most primitive melt compositions in equilibrium with clinopyroxenes. Vertical broken bars represent average TMFs excluding the highest TMF data in GT1A.

Table 4. Estimated trapped melt fractions of gabbroic core samples from Hole GT1A and GT2A.

Hole_Core_Section_Interval	n	mbs		Cpx compositions [µg/g]			Equilibrium melt [µg/g]			Whole rocks [µg/g]			X-mass fraction					%TMF	
		Top	Bottom	La	Ce	Pr	La	Ce	Pr	La	Ce	Pr	Ol	Plag	Cpx	TMF	Total X	Average	STDEV
Hole GT1A based on the minimum La in Cpx core																			
GT1A_30_4_59-63_min	3	72.75	72.79	0.146	0.862	0.205	2.710	10.042	1.369	0.218	0.647	0.110	0.050	0.862	0.050	0.038	1.000		
GT1A_30_4_63-67_min	3	72.79	72.83	0.078	0.522	0.117	1.440	6.081	0.779	0.372	1.443	0.303	0.050	0.059	0.696	0.195	1.000		
GT1A_38_1_52-56_min	3	91.67	91.71	0.132	0.698	0.172	2.435	8.141	1.149	0.172	0.653	0.129	0.050	0.268	0.650	0.032	1.000		
GT1A_38_4_48-52_min	3	94.06	94.10	0.123	0.681	0.162	2.281	7.937	1.082	0.205	0.732	0.141	0.150	0.413	0.380	0.057	1.000		
GT1A_41_3_33-37_min	3	99.34	99.38	0.132	0.775	0.167	2.436	9.034	1.114	0.113	0.437	0.092	0.320	0.300	0.363	0.017	1.000		
GT1A_45_2_43-47_min	3	104.72	104.76	0.204	1.202	0.299	3.784	14.009	1.992	0.199	0.655	0.126	0.100	0.743	0.139	0.017	1.000		
GT1A_83_1_62-66_min	3	206.82	206.86	0.208	1.238	0.292	3.852	14.423	1.946	0.192	0.622	0.131	0.150	0.684	0.152	0.015	1.000		
GT1A_95_2_38-42_min	3	237.17	237.21	0.159	1.055	0.275	2.939	12.290	1.833	0.429	1.176	0.221	0.200	0.577	0.150	0.073	1.000		
GT1A_152_4_13-17_min	3	392.47	392.51	0.177	0.915	0.213	3.284	10.669	1.418	0.190	0.628	0.126	0.150	0.526	0.299	0.026	1.000	3.44	2.09
Hole GT1A based on the average value of La in Cpx core																			
GT1A_30_4_59-63_average	3	72.75	72.79	0.152	0.896	0.216	2.819	10.439	1.439	0.218	0.647	0.110	0.050	0.865	0.050	0.035	1.000		
GT1A_30_4_63-67_average	3	72.79	72.83	0.111	0.724	0.177	2.058	8.433	1.182	0.372	1.443	0.303	0.050	0.268	0.552	0.131	1.000		
GT1A_38_1_52-56_average	3	91.67	91.71	0.141	0.735	0.175	2.603	8.566	1.166	0.172	0.653	0.129	0.050	0.388	0.530	0.032	1.000		
GT1A_38_4_48-52_average	3	94.06	94.10	0.140	0.791	0.195	2.598	9.224	1.298	0.205	0.732	0.141	0.150	0.495	0.308	0.046	1.000		
GT1A_41_3_33-37_average	3	99.34	99.38	0.170	0.911	0.202	3.147	10.623	1.345	0.113	0.437	0.092	0.350	0.300	0.340	0.011	1.000		
GT1A_45_2_43-47_average	3	104.72	104.76	0.243	1.324	0.333	4.492	15.432	2.217	0.199	0.655	0.126	0.100	0.695	0.194	0.011	1.000		
GT1A_83_1_62-66_average	3	206.82	206.86	0.213	1.257	0.302	3.946	14.656	2.013	0.192	0.622	0.131	0.150	0.681	0.155	0.014	1.000		
GT1A_95_2_38-42_average	3	237.17	237.21	0.173	1.099	0.289	3.207	12.807	1.926	0.429	1.176	0.221	0.200	0.581	0.150	0.069	1.000		
GT1A_152_4_13-17_average	3	392.47	392.51	0.227	1.042	0.230	4.201	12.146	1.532	0.190	0.628	0.126	0.150	0.443	0.392	0.015	1.000	2.91	2.07

Table 4. (Continued)

Hole_Core_Section_Interval	n	mbs Top	mbs Bottom	Cpx compositions [μg/g] La	Ce	Pr	Equilibrium melt [μg/g] La	Ce	Pr	Whole rocks [μg/g] La	Ce	Pr	X-mass fraction Ol	Plag	Cpx	TMF	Total X	%TMF Average	STDEV
Hole GT2A based on the minimum La in Cpx core																			
GT2A_20_3_55-59_min	3	44.47	44.51	0.303	1.535	0.398	5.610	17.886	2.653	0.528	1.639	0.297	0.020	0.750	0.165	0.065	1.000		
GT2A_35_3_71-75_min	3	90.08	90.12	0.341	1.556	0.381	6.306	18.132	2.538	0.348	1.223	0.251	0.050	0.702	0.209	0.040	1.000		
GT2A_46_3_56-60_min	3	120.30	120.34	0.296	1.481	0.348	5.479	17.258	2.321	0.287	1.174	0.250	0.100	0.630	0.229	0.041	1.000		
GT2A_46_4_47-51_min	3	121.17	121.21	0.269	1.436	0.366	4.983	16.733	2.437	0.346	1.148	0.223	0.020	0.879	0.055	0.046	1.000		
GT2A_50_1_47-51_min	3	130.75	130.79	0.220	1.200	0.299	4.078	13.982	1.994	0.267	0.737	0.123	0.050	0.868	0.050	0.032	1.000		
GT2A_52_3_25-29_min	3	138.31	138.35	0.303	1.697	0.445	5.606	19.774	2.964	0.238	0.645	0.104	0.150	0.783	0.055	0.012	1.000		
GT2A_75_3_8-12_min	3	196.52	196.56	0.229	1.298	0.349	4.242	15.130	2.330	0.181	0.567	0.105	0.150	0.775	0.057	0.018	1.000		
GT2A_86_2_33-37_min	3	229.03	229.07	0.189	1.073	0.273	3.504	12.508	1.822	0.197	0.760	0.166	0.020	0.819	0.124	0.037	1.000		
GT2A_102_1_3-7_min	3	273.88	273.92	0.147	0.757	0.191	2.731	8.825	1.270	0.174	0.584	0.114	0.200	0.637	0.112	0.051	1.000		
GT2A_104_1_5-9_min	3	280.00	280.04	0.178	0.965	0.257	3.288	11.251	1.714	0.246	0.746	0.132	0.050	0.798	0.107	0.045	1.000		
GT2A_104_4_53-57_min	3	282.73	282.77	0.253	1.339	0.315	4.687	15.609	2.098	0.273	0.926	0.178	0.100	0.732	0.132	0.036	1.000		
GT2A_105_2_39-43_min	3	284.25	284.29	0.236	1.304	0.357	4.363	15.199	2.381	0.211	0.726	0.140	0.050	0.818	0.108	0.024	1.000		
GT2A_117_2_6-10_min	3	314.34	314.38	0.311	1.858	0.466	5.758	21.651	3.107	0.316	1.096	0.214	0.050	0.766	0.108	0.023	1.000	3.61	1.45
Hole GT2A based on the average value of La in Cpx core																			
GT2A_20_3_55-59_average	3	44.47	44.51	0.385	1.931	0.475	7.135	22.504	3.165	0.528	1.639	0.297	0.020	0.775	0.160	0.045	1.000		
GT2A_35_3_71-75_average	3	90.08	90.12	0.382	1.850	0.461	7.082	21.564	3.073	0.348	1.223	0.251	0.050	0.770	0.150	0.030	1.000		
GT2A_46_3_56-60_average	3	120.30	120.34	0.330	1.508	0.364	6.114	17.572	2.425	0.287	1.174	0.250	0.100	0.601	0.265	0.033	1.000		
GT2A_46_4_47-51_average	3	121.17	121.21	0.301	1.521	0.399	5.580	17.727	2.659	0.346	1.148	0.223	0.020	0.889	0.050	0.041	1.000		
GT2A_50_1_47-51_average	3	130.75	130.79	0.239	1.305	0.341	4.418	15.215	2.271	0.267	0.737	0.123	0.050	0.873	0.050	0.027	1.000		
GT2A_52_3_25-29_average	3	138.31	138.35	0.330	1.815	0.482	6.118	21.152	3.213	0.238	0.645	0.104	0.150	0.790	0.050	0.010	1.000		
GT2A_75_3_8-12_average	3	196.52	196.56	0.264	1.383	0.362	4.883	16.113	2.411	0.181	0.567	0.105	0.150	0.785	0.050	0.015	1.000		
GT2A_86_2_33-37_average	3	229.03	229.07	0.231	1.169	0.290	4.276	13.620	1.936	0.197	0.760	0.166	0.020	0.840	0.110	0.030	1.000		
GT2A_102_1_3-7_average	3	273.88	273.92	0.160	0.805	0.199	2.957	9.387	1.328	0.174	0.584	0.114	0.200	0.627	0.126	0.047	1.000		
GT2A_104_1_5-9_average	3	280.00	280.04	0.217	1.067	0.266	4.014	12.434	1.774	0.246	0.746	0.132	0.050	0.815	0.100	0.035	1.000		
GT2A_104_4_53-57_average	3	282.73	282.77	0.273	1.450	0.347	5.060	16.899	2.314	0.273	0.926	0.178	0.100	0.760	0.108	0.032	1.000		
GT2A_105_2_39-43_average	3	284.25	284.29	0.239	1.351	0.368	4.429	15.744	2.451	0.211	0.726	0.140	0.050	0.813	0.115	0.022	1.000		
GT2A_117_2_6-10_average	3	314.34	314.38	0.343	1.979	0.494	6.358	23.063	3.293	0.316	1.096	0.214	0.050	0.766	0.165	0.019	1.000	2.97	1.12

32   The magmatic conditions and hypersolidus deformation of lower crustal magma chamber
        below a fast-spreading ridge ─ Insight from the core analyses of the Oman ICDP drill holes
        GT1A & GT2A

5   Discussion

Downhole textural variations of GT1A and GT2A core samples

A hybrid magma chamber consisting of the upper crystal mush and the lower sheeted sills has been proposed beneath the Oman paleospreading ridge on the basis of field observations, microstructural analyses and theoretical considerations regarding the formation of the lower crustal gabbros (Boudier et al., 1996; Chenevez et al., 1997; Kelemen and Aharonov, 1998; Nicolas and Boudier, 2015b). Mock et al. (2021) and Koepke et al. (2022) divided the 5 km thick lower crustal gabbros exposed along the Wadi Gideah into four units, the Dike/Gabbro Transition, Upper Foliated Gabbro, Lower Foliated Gabbro and Layered Gabbro, in descending order, where the upper foliated gabbro was solidified crystal mushes subsided from the axial melt lens, and the Lower Foliated and Layered Gabbros formed by sheeted sills intruded in-situ within the lower crust. According to their stratigraphic subdivision, the upper GT2A and the lower GT1A is correlated to the transitional level from Foliated to Layered Gabbro Unit and the lower Layered Gabbro Unit, respectively.   The fabric strength of plagioclase and clinopyroxene shows moderate lineation from Dike-Gabbro Transition through the Upper Foliated Gabbro Unit (Mock et al., 2021). Foliation develops in the Lower Foliated Gabbro to the uppermost Layered Gabbro Unit, where girdle distributions in [100] and point maxima in (010) develop, with the lineation component becoming stronger down section through the Layered Gabbro Unit. Mock et al. (2021) ascribed the lineation fabric in the Dike-Gabbro Transition and the Upper Foliated Gabbro Unit to the subvertical subsidence of crystal mushes from the axial melt lens (AML), and the foliation in the Lower Foliated Gabbro and the Layered Gabbro Unit to a compaction-induced fabric (VanTongeren et al., 2015; Mock et al., 2021). The increasing lineation from the Lower Layered Gabbro to the Moho Transition Zone is interpreted to result from drag shearing by the convecting mantle.

Smaller mean grain size of plagioclase and clinopyroxene in and above the Lower Foliated Gabbro than in the Layered Gabbro is explained as the consequence of faster cooling rates in the AML, however, the deformation regime change is proposed between the Upper Foliated to Lower Foliated Gabbro (Mock et al., 2021). Furthermore, the environment within the subsiding crystal mush is compatible with the downward increase in crystal lattice orientation (CPO) strength from the Lower Foliated to Layered Gabbro Unit (Mock et al., 2021). The abundance of primary plagioclase sharply drops within the upper 100 m of GT2A, and then gradually decreases downhole further below and through GT1A (Figure 4c, 4d). Likewise, broken plagioclase crystals sharply increase in the uppermost 100 m in GT2A and gradually increase in abundance further below to the bottom of GT1A. At the same time, the shape of plagioclase changes from thin to thick plates with linear outlines and concentric zoning to stubby broken crystals with undulose outlines. The aspect ratio of primary plagioclase is highest at the top of the hole GT2A and rapidly decreases to 2.0 within the uppermost 200 m, and then remains unchanged throughout the hole GT1A (Figure 4a, 4b). Meanwhile, clinopyroxene is deformed to distorted rectangular shapes with a quarter structure, and then changes downhole into crystals with sub-grains, which eventually forms neoblasts (Figure 2). Texturally equilibrated polygonal clinopyroxene that meet at a triple junction of obtuse angles around 120° increases in number in lower GT1A. As such, the variations in microstructure occurs progressively from the hole GT2A down through GT1A. These textural changes of plagioclase and clinopyroxene from GT2A down through GT1A indicate progressive deformation under submagmatic conditions downhole, followed by subsolidus crystal lattice deformation, most likely caused by compaction of the crystal mush. The

TMF remains constant between 1 mass% and 5 mass% throughout both holes, except for the peak at the top of each hole, indicating that mechanical compaction of the crystal mush reached its maximum level (Figure 9). Deformation of crystal mush under a hypersolidus condition could cause rotation and sliding of platy and prismatic cumulus crystals with small melt fractions as low as 10-15 vol% (Nicolas, 1992). Under lower melt fraction, further deformation is accommodated by solid-state flow that causes crystal lattice warping, dislocation creep and grain boundary migration. This resulted in the deformation twinning of plagioclase and quarter structure, subgrains and neoblasts shown by clinopyroxene. If such compaction occurred in the subsiding crystal mush, lower gabbros suffered longer periods of cooling and therefore, have sufficient time for recrystallized crystals to attain textural equilibration as suggested by the very low cooling rate of 0.0001 °C/a (Coogan et al., 2007). Ophitic clinopyroxenes are present throughout the two drill holes irrespective of the stratigraphic levels, although they gradually decrease in number downhole. They are typically observed in the sheeted dikes and the upper gabbros, where the cooling rate is much higher than 0.0001 °C/a due to intense hydrothermal circulation. This suggests that gabbros from both holes crystallized under large degrees of supercooling identical to the roof zone of the AML, and were then transported downward through the subsiding crystal mush in the lower crust.

The whole-rock and mineral compositions

The whole-rock major element compositions of gabbros from two drill holes are plotted together with core compositions of constituent olivine, plagioclase and clinopyroxene (Figure 10). Also plotted are the whole-rock compositions of the V-1 sheeted dikes (Umino et al., 2003; Miyashita et al., 2003; Fudai, 2018) and gabbros from the Pito Deep (Perk et al., 2007) and the Hess Deep (Gillis et al., 2014).   As is expected for the cumulate origin, the ICDP gabbro core samples plot within the triangles connecting olivine, plagioclase and clinopyroxene in Al_2O_3-MgO and CaO-MgO compositional spaces (Figure 10a, 10b). However, some gabbro core samples plot outside of the olivine-plagioclase-clinopyroxene triangle in the FeO-MgO plot but within a quadrilateral including the sheeted dikes and the constituent minerals (Figure 10c). This indicates that the gabbro core compositions consist of not only cumulus minerals but also a small amount of melts as represented by the several mass% TMFs. These trapped melts are generally more differentiated as shown by the melt compositions estimated from the coexisting clinopyroxene rims (Figure 6). Although most melt compositions in equilibrium with the clinopyroxenes overlap the sheeted dike compositions, some melts estimated from GT1A clinopyroxene cores are more primitive. This suggests the presence of primitive melt that neither extrudes on the surface nor intrudes into the upper crust but remains below the AML to form the lower crust.

The relationships of An mol% of plagioclase versus Mg# of clinopyroxene show that the Oman gabbros are higher in An at a given clinopyroxene Mg# than the Pito Deep gabbros (Figure 7b). Although the Hess Deep gabbros are also lower in An than the Oman gabbros with higher Mg# >83, they are largely scatter and overlap each other in lower Mg#<83. These relationships suggest hydrous conditions for the Oman paleoridge magma (Koepke et al., 2022). However, plagioclase and clinopyroxene pairs from island arc gabbros plot in a much higher An region than those of the Oman gabbros, suggesting that the Oman paleoridge environment is less hydrous compared to true arc settings. In contrast to common normal zonings of clinopyroxenes in Oman gabbros, reversely zoned plagioclase is not rare. This is explained by the enrichment of water in the residue melts that crystallized the An-rich rims of plagioclase, but did not affect clinopyroxene Mg# (Koepke et al., 2022).

34   The magmatic conditions and hypersolidus deformation of lower crustal magma chamber
below a fast-spreading ridge — Insight from the core analyses of the Oman ICDP drill holes
GT1A & GT2A

Although the overall whole-rock and mineral compositions of the upper GT2A gabbros are more differentiated than the lower GT1A gabbros, the compositional variations of both holes are similarly large and largely overlap each other, showing neither constant increase nor decrease by stratigraphy, except the uppermost 150 m in hole GT2A (Figures 5, 8). Compared to clinopyroxenes of the same stratigraphic levels along Wadi Gideah section (Koepke et all., 2022), clinopyroxenes in hole GT2A show similar ranges and those in GT1A show larger variations. Koepke et al. (2022) argued that olivine, plagioclase and clinopyroxene show an overall differentiation trend upward from Layered Gabbro through the Upper Foliated Gabbro, an upward magmatic differentiation expected in the interior of a magma chamber composed of sheeted sills. However, more densely sampled clinopyroxenes in GT1A gabbro cover the widest range of Mg#, Cr_2O_3 and TiO_2 exhibited by the clinopyroxenes in the Wadi Gideah Layered Gabbro. Thus, the "upward differentiation trend" of the layered gabbro section may be due in part to the shortage of sampling. Highly scattered compositional variations shown by the Dike-Gabbro Transition through the Upper Foliated Gabbro span the most primitive compositions in the lowermost layered gabbros, indicating the delivery of primitive magma to the AML (Koepke et all., 2022). The high proportion of primary plagioclase and clinopyroxene in the uppermost GT2A suggests that the crystal mush suffered less compaction at higher stratigraphic levels and that more interstitial melts remain between cumulus crystals. This may explain the highly varied composition for the upper gabbros.
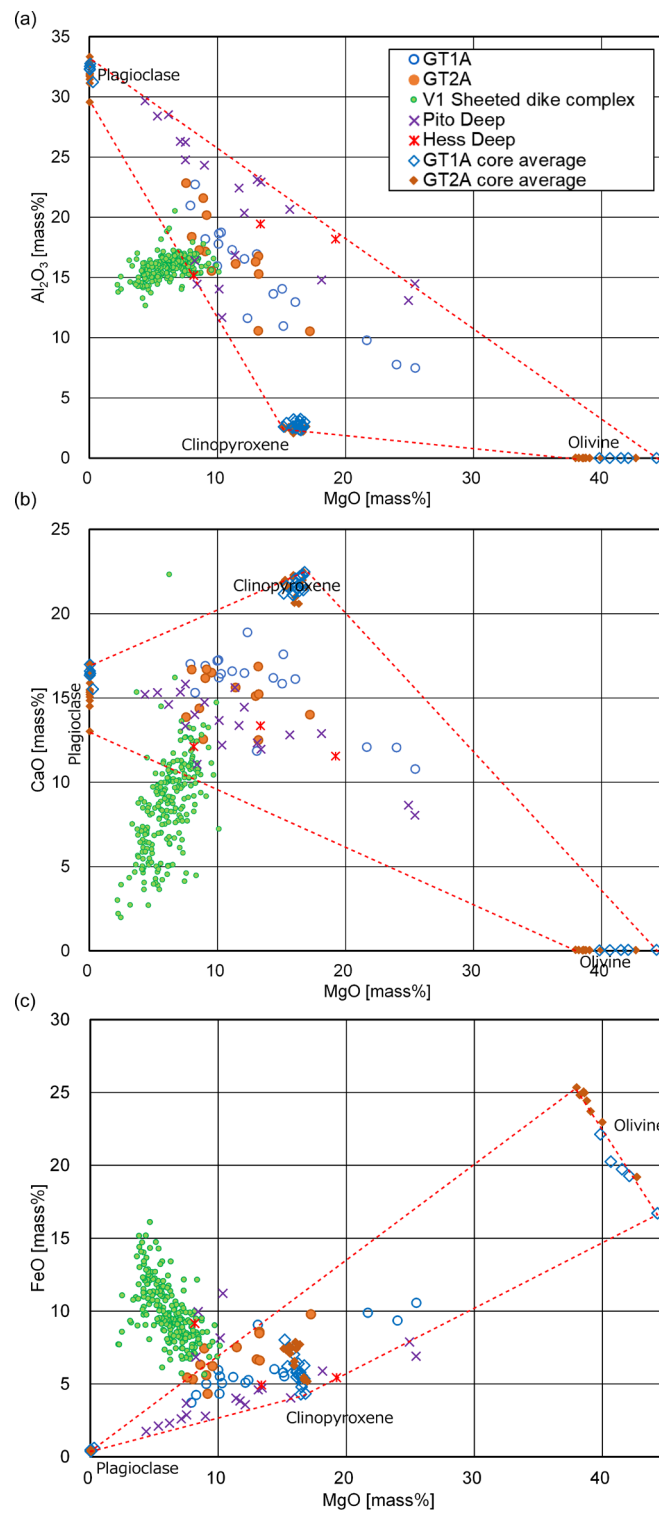
Figure 10. Al$_2$O$_3$ (a), CaO (b) and FeO (c) plotted against MgO of the whole-rock compositions and average core compositions of olivine, clinopyroxene and plagioclase of gabbroic core samples from Hole GT1A and GT2A. Also plotted are the V1 sheeted dikes (small circles; Umino et al., 2003; Miyashita et al., 2003; Fudai, 2018) and gabbroic samples from the Pito Deep (crosses; Perk et al., 2007) and Hess Deep (asterisks; Gillis et al., 2014).

36   The magmatic conditions and hypersolidus deformation of lower crustal magma chamber
below a fast-spreading ridge ― Insight from the core analyses of the Oman ICDP drill holes
GT1A & GT2A

6   Conclusions

Microscopic observations demonstrate progressive textural variations of plagioclase and clinopyroxene from Hole GT2A to Hole GT1A. Primary igneous plagioclase rapidly decreases in number with reducing aspect ratios and broken plagioclase increases in abundance downhole in the upper GT2A, followed by a steady decrease in primary clinopyroxene through Hole GT1A, and increases in recrystallized plagioclase and clinopyroxene subgrains and neoblasts. These textural changes indicate progressive deformation under submagmatic conditions downhole, followed by subsolidus crystal lattice deformation, most likely caused by compaction of the crystal mush. The consistently low TMFs of less than 5 mass% indicate that the crystal mush has reached its maximum level of compaction. The trapped melts in closed interstices between cumulus crystals crystallized normally zoned rims of clinopyroxene. However, reversely zoned cumulus plagioclase crystallized from hydrous residual melts. The whole-rock and mineral compositions do not evolve with stratigraphy but vary in a similar range through holes GT2A and GT1A besides the upper GT2A. The presence of ophitic clinopyroxene throughout both holes indicates the crystallization under large degrees of supercooling, consistent with the subsiding crystal mush origin for these gabbro cores.

Acknowledgements

Appendix

The supplementary materials are available from T.N. upon request.

References

Adachi, Y. and Miyashita, S. (2003) Geology and petrology of the plutonic complexes in the Wadi Fizh area: Multiple magmatic events and segment structure in the northern Oman ophiolite. Geochemistry, Geophysics, Geosystems 4, 8619, doi:10.1029/2001GC000272, 9.

Alt, J.C., Kinoshita, H., Stokking, L.B., Allerton, S., Bach, W., Becker, K., Boehm, V.K., Brewer, T.S., Dilek, Y., Filice, F., Fisk, M.R., Fujisawa, H., Fumes, H., Querin, Q., Harper, G.D., Honnorez, J., Hoskins, H., Ishizuka, H., Laveme, C., McNeill, A.W., Magenheim, A.J., Miyashita, S., Pezard, P.A., Salisbury, M.H., Tartarotti, P., Teagle, D.A., Vanko, D.A., Wilkens, R.H., and Worm, H.U. (1993) Proceeding of the Ocean Drilling Program, Initial Reports 148: College Station, TX (Ocean Drilling Program), https://doi:10.2973/odp.proc.ir.148.1993p.

Blackman, D.K., ldefonse, B., John, B.E., Ohara, Y., Miller, D.J., Abe, N., Abratis, M., Andal, E.S., Andreani, M., Awaji, S., Beard, J.S., Brunelli, D., Charney, A.B., Christie, D.M., Collins, J., Delacour, A.G., Delius, H., Drouin, M., Einaudi, F., Escartín, J., Frost, B.R., FrühGreen, G., Fryer, P.B., Gee, J.S., Godard, M., Grimes, C.B., Halfpenny, A., Hansen, H.E., Harris, A.C., Tamura, A., Hayman, N.W., Hellebrand, E.X., Hirose, T., Hirth, J.G., Ishimaru, S., Johnson, K.T.M., Karner, G.D., Linek, M., MacLeod, C.J., Maeda, J., Mason, O.U., McCaig, A.M., Michibayashi, K., Morris, A., Nakagawa, T., Nozaka, T., Rosner, M., Searle,

R.C., Suhr, G., Tominaga, M., von der Handt, A., Yamasaki, T., and Zhao, X. (2011) Drilling constraints on lithospheric accretion and evolution at Atlantis Massif, Mid-Atlantic Ridge 30°N. Journal of Geophysical Reserach 116, B07103, doi:10.1029/2010JB007931.

Brandy, J.B. and McCallister, R.H. (1983) Diffusion data for clinopyroxenes from homogenization and self-diffusion experiments. American Mineralogist 68, 95-105, 003-004X/83/0102-0095$02.00.

Cheadle, M.J. and Gee, J.S. (2017) Quantitative Textural Insights into the Formation of Gabbro in Mafic Intrusions. Elements 13, 403–408.

Chenevez, J. and Nicolas, A. (1997) Crustal feeding in the Oman ophiolite: from the top and from the bottom? A thermal and mass balance model. Geophysical Research Letters 24, 1811–1514.

Chenevez, J., Machetel, P., and Nicolas, A. (1998) Numerical magma chambers in the Oman ophiolite. Journal of Geophysical Research 103, 15443–15455.

Cherniak, D.J. and Liang, Y. (2012) Ti diffusion in natural pyroxene. Geochimica et Cosmochimica Acta 98, 31-47, http://dx.doi.org//10.1016/j.gca.2012.09.02.

Coogan, L.A., Jenkin, G.R.T., and Wilson, R.N. (2007) Contrasting Cooling Rates in the Lower Oceanic Crust at Fast- and Slow-spreading Ridges Revealed by Geospeedometry. Journal of Petrology 48, 2211–2231, doi: 10.1093/petrology/egm057.

Dick, H.J.B. and Natland, J.H. (1996) Late-stage melt evolution and transport in the shallow mantle beneath the East Pacific Rise. Proceedings of the Ocean Drilling Program, Scientific Results 147, 103-134.

Dick, H.J.B., Natland, J.H., Alt, J.C., Bach, W., Bideau, D., Gee, J.S., Haggas, S., Hertogen, J.G.H., Hirth, G., Holm, P.M., Ildefonse, B., Iturrino, G.J., John, B.E., Kelley, D.S., Kikawa , E., Kingdon, A., LeRoux, P.J., Maeda, J., Meyer, P.S., Miller, D.J., Naslund, H.R., Niu, Y.L., Robinson, P.T., Snow, J., Stephen, R.A., Trimby, P.W., Worm, H.U., and Yoshinobu, A. (2000) A long in situ section of the lower ocean crust: results of ODP Leg 176 drilling at the Southwest Indian Ridge. Earth and Planetary Science Letters 179, 31-51.

Garbe-Schönberg, D., Koepke, J., Müller, S., Mock, D., and Müller, T. (2022) A Reference Section Through Fast-Spread Lower Oceanic Crust, Wadi Gideah, Samail Ophiolite (Sultanate of Oman): Whole Rock Geochemistry. Journal of Geophysical Research 127, e2021JB022734, https://doi.org/10.1029/2021JB022734.

Gillis, K.M., Me´vel, C., and Allan, J. (1993) Proceeding of the Ocean Drilling Program, Initial Reports 147: College Station, TX (Ocean Drilling Program).

Gillis, K. M., Snow, J. E., Klaus, A., Abe, N., Adrião, A.B., Akizawa, N., Ceuleneer, G., Cheadle, M.J., Faak, K., Falloon, T.J., Friedman, S.A., Godard, M., Guerin, G., Harigane, Y., Horst, A.J., Hoshide, T., Ildefonse, B., Jean, M.M., John, B.E., Koepke, J., Machi, S., Maeda, J., Marks, N.E., McCaig, A.M., Meyer, R., Morris, A., Nozaka, T., Python, M., Saha, A., and Wintsch, R.P. (2014) Primitive layered gabbros from fast-spreading lower oceanic crust. Nature 505, 204–207, https://doi:10.1038/nature12778.

Haase, K.M., Lima, S., Krumm, S., and Dieter, G.S. (2014) The magmatic evolution of young island arc crust observed in gabbroic to tonalitic xenoliths from Raoul Island, Kermadec Island Arc. Lithos 210-211, 199-208.

Ichiyama, Y., Morishita, T., Tamura, A., and Arai, S. (2013) Petrology of peridotite xenolith-bearing basaltic to andesitic lavas from the Shiribeshi Seamount, off northwestern Hokkaido, the Sea of Japan. Journal of Asian Earth Sciences 76, 48–58.

Jochum, K.P., Nohl, U., Herwig, K., Lammel, E., Stoll, B., and Hofmann, A.W. (2005) GeoReM: A New Geochemical Database for Reference Materials and Isotopic Standards. Geostandards and Geoanalytical Research 29, 333-338, https://doi.org/10.1111/j.1751-908X.2005.tb00904.x.

Jochum, K.P. and Nohl, U. (2008) Reference materials in geochemistry and environmental research and the

38   The magmatic conditions and hypersolidus deformation of lower crustal magma chamber
below a fast-spreading ridge — Insight from the core analyses of the Oman ICDP drill holes
GT1A & GT2A

GeoReM database. Chemical Geology 253, 50-53.

Karson, J. A. (2002) Geologic Structure of the Uppermost Oceanic Crust Created at Fast- to Intermediate-Rate Spreading Centers. Annual Review of Earth and Planetary Sciences 30, 347–384, https://doi:10.1146/annurev.earth.30.091201.141132.

Kelemen, P.B. and Aharonov, E. (1998) Periodic Formation of Magma Fractures and Generation of Layered Gabbros in the Lower Crust Beneath Oceanic Spreading Ridges. Faulting and Magmatism at Mid-Ocean Ridges 106, https://doi.org/10.1029/GM106p0267.

Kelemen, P.B., Matter, J.M., Teagle, D.A.H., Coggon, J.A., and the Oman Drilling Project Science Team. (2020a) Introduction to Science Theme 1A: gabbro traverse. Proceedings of the Oman Drilling Project: College Station, TX (International Ocean Discovery Program), https://doi.org/10.14379/OmanDP.proc.105.2020

Kelemen, P.B., Matter, J.M., Teagle, D.A.H., Coggon, J.A., and the Oman Drilling Project Science Team. (2020b) Site GT1: layered cumulate gabbros and deep fault zones. Proceedings of the Oman Drilling Project: College Station, TX (International Ocean Discovery Program), https://doi.org/10.14379/OmanDP.proc.106.2020

Kelemen, P.B., Matter, J.M., Teagle, D.A.H., Coggon, J.A., and the Oman Drilling Project Science Team. (2020c) Site GT2: transition from foliated to layered gabbros. Proceedings of the Oman Drilling Project: College Station, TX (International Ocean Discovery Program), https://doi.org/10.14379/OmanDP.proc.107.2020

Koepke, J., Garbe-Schönberg, D., Müller, T., Mock, D., Müller, S., and Nasir, S. (2022) A Reference Section Through Fast-Spread Lower Oceanic Crust, Wadi Gideah, Samail Ophiolite (Sultanate of Oman): Petrography and Petrology. Journal of Geophysical Research 127, e2021JB022735, https://doi.org/10.1029/2021JB022735

Kusano, Y., Hayashi, M., Adachi, Y., Umino, S., and Miyashita, S. (2014) Evolution of volcanism and magmatism during initial arc stage: constraints on the tectonic setting of the Oman Ophiolite. Geological Society, London, Special Publications 392, 177-193.

Lissenberg, C.J., MacLeod, C.J., Howard, K.A., and Godard, M. (2013) Pervasive reactive melt migration through fast-spreading lower oceanic crust (Hess Deep, equatorial Pacific Ocean). Earth and Planetary Science Letters 361, 436-447.

Longerich, H.P., Jackson, S.E., and Gunther, D. (1996) Laser Ablation Inductively Coupled Plasma Mass Spectrometric Transient Signal Data Acquisition and Analyte Concentration Calculation. Journal of Analytical Atomic Spectrometry 11, 899–904.

MacLeod, C.J. and Yaouancq, G. (2000) A fossil melt lens in the Oman ophiolite: Implications for magma chamber processes at fast spreading ridges. Earth and Planetary Science Letters 176, 357–373.

Marsh, B.D. (1996) Solidification fronts and magmatic evolution. Mineralogical Magazine 60, 5–40.

Miller, D.J., Iturrino, G.J., and Christensen, N.I. (1996) Geochemical and petrological constraints on velocity behavior of lower crustal and upper mantle rocks from the fast-spreading ridge at Hess Deep. Proceedings of the Ocean Drilling Program, Scientific Results 147.

Miyashita, S., Adachi, Y., and Umino, S. (2003) Along-axis magmatic system in the northern Oman ophiolite: Implications of compositional variation of the sheeted dike complex. Geochemistry, Geophysics, Geosystems 4, 8617, doi:10.1029/2001GC000235, 9.

Mock, D., Ildefonse, B., Müller, T., and Koepke, J. (2021) A Reference Section Through Fast-Spread Lower Oceanic Crust, Wadi Gideah, Samail Ophiolite (Sultanate of Oman): Insights From Crystallographic Preffered Orientations. Journal of Geophysical Research 126, e2021JB021864, https://doi.org/10.1029/2021JB021864.

Morishita, T., Ishida, Y., and Arai, S. (2005a) Simultaneous determination of multiple trace element compositions in thin (<30 μm) layers of BCR-2G by 193 nm ArF excimer laser ablation-ICP-MS: implications for matrix effect and elemental fractionation on quantitative analysis. Geochemical Journal 39, 327–340.

Morishita, T., Ishida, Y., Arai, S., and Shirasaka, M. (2005b) Determination of Multiple Trace Element Compositions in Thin (30 μm) Layers of NIST SRM 614 and 616 Using Laser Ablation-Inductively Coupled Plasma-Mass Spectrometry (LA-ICP-MS). Geostandards and Geoanalytical Research 29, 107-122.

Müller, S., Garbe-Schönberg, D., Koepke, J., and Hoernle, K. (2022) A Reference Section Through Fast-Spread Lower Oceanic Crust, Wadi Gideah, Samail Ophiolite (Sultanate of Oman): Trace Element Systematics and REE Crystallization Temperatures—Implications for Hybrid Crustal Accretion. Journal of Geophysical Research 127, e2021JB022699, https://doi.org/10.1029/2021JB022699.

Natland, J.H. and Dick, H.J.B. (1996) Melt Migration through High-Level Gabbroic Cumulates of the East Pacific Rise at Hess Deep: The Origin of Magma Lenses and the Deep Crustal Structure of Fast-Spreading Ridges. Proceedings of the Ocean Drilling Program, Scientific Results 147.

Nicols, A. (1992) Kinematics in Magmatic Rocks with Special Reference to Gabbros. Journal of Petrology 33, 891–915, https://doi.org/10.1093/petrology/33.4.891.

Nicolas, A., Boudier, F., and Ildefonse, B. (1996) Variable crustal thickness in the Oman ophiolite: Implication for oceanic crust. Journal of Geophysical Research 101, 17941–17950, https://doi.org/10.1029/96JB00195.

Nicolas, A. and Ildefonse, B. (1996) Flow mechanism and viscosity in basaltic magma chambers. Geophysical Research Letters 23, 2013–2016.

Nicolas, A., Boudier, F., Ildefonse, B., and Ball, E. (2000) Accretion of Oman and United Arab Emirates ophiolite—Discussion of a new structural map. Marine Geophysical Researches 21, 147–180, https://doi.org/10.1023/A:1026769727917.

Nicolas, A. and Boudier, F. (2015a) Inside the magma chamber of a dying ridge segment in the Oman ophiolite. Terra Nova 27, 69–76, https://doi: 10.1111/ter.12130.

Nicolas, A. and Boudier, F. (2015b) Structural contribution from the Oman ophiolite to processes of crustal accretion at the East Pacific Rise. Terra Nova 27, 77–96, doi: 10.1111/ter.12137.

Noguchi, S., Morishita, T., and Toramaru, A. (2004) Corrections for Na-loss on micro-analysis of glasses by electron probe X-ray micro analyzer. Japanese Magazine of Mineralogical and Petrological Sciences 33, 85–95.

Pallister, J.S. and Hopson, C.A. (1981) Samail Ophiolite plutonic suite: Field relations, phase variation, cryptic variation and layering, and a model of a spreading ridge magma chamber. Journal of Geophysical Research 86, 2593–2644, doi:10.1029/JB086iB04p02593.

Perk, N.W., Coogan, L.A., Karson, J.A., Klein, E.M., and Hanna, H.D. (2007) Petrology and geochemistry of primitive lower oceanic crust from Pito Deep: implications for the accretion of the lower crust at the Southern East Pacific Rise. Contributions to Mineralogy and Petrology 154, 575–590.

Quick, J.E. and Denlinger, R. (1993) Ductile deformation and the origin of layered gabbro in ophiolites. Journal of Geophysical Research 98, 14015–14027.

Rioux, M., Bowring, S., Kelemen, P., Gordon, S., Miller, R., and Dudás, F. (2013) Tectonic development of the Samail ophiolite: High-precision U-Pb zircon geochronology and Sm-Nd isotopic constraints on crustal growth and emplacement. Journal of Geophysical Research 118, 2085–2101, doi:10.1002/jgrb.50139.

Smith, A.G. (1971) Alpine Deformation and the Oceanic Areas of the Tethys, Mediterranean and Atlantic.

40   The magmatic conditions and hypersolidus deformation of lower crustal magma chamber
below a fast-spreading ridge — Insight from the core analyses of the Oman ICDP drill holes
GT1A & GT2A

Bulletin Geological Society of America 82, 2039-2070.

Sun, S.S. and McDonough, W.F. (1989) Chemical and isotopic systematics of oceanic basalts: implications for mantle composition and processes. Geological Society, London, Special Publications 42, 313-345.

Teagle, D.A.H., Ildefonse, B., Blum, P., and the IODP Expedition 335 Scientists. (2012) IODP expedition 355: deep sampling in ODP hole 1256D. Scientific Drilling 13, 28-34.

Tollan, P.M.E., Bindeman, I., and Blundy, J.D. (2012) Cumulate xenoliths from St. Vincent, Lesser Antilles Island Arc: a window into upper crustal differentiation of mantle-derived basalts. Contributions to Mineralogy and Petrology 163, 189-208.

Umino, S., Miyashita, S., Hotta, F., and Adachi, Y. (2003) Along-strike variation of the sheeted dike complex in the Oman Ophiolite: Insights into subaxial ridge segment structures and the magma plumbing system. Geochemistry, Geophysics, Geosystems 4, 8618, doi:10.1029/2001GC000233, 9.

Van Orman, J.A., Grove, T.L., and Shimizu, N. (2001) Rare earth element diffusion in diopside: influence of temperature, pressure, and ionic radius, and an elastic model for diffusion in silicates. Contributions to Mineralogy and Petrology 141, 687-703, doi: 10.1007/s004100100269.

Van Tongeren, J.A., Kelemen, P.B., and Hanghoj, K. (2008) Cooling rates in the lower crust of the Oman ophiolite: Ca in olivine, revisited. Earth and Planetary Science Letters 267, 69 - 82.

Workman, R.K. and Hart, S.R. (2005) Major and trace element composition of the depleted MORB mantle (DMM). Earth and Planetary Science Letters 231, 53-72.